

A Billion-scale Foundation Model for Remote Sensing Images

Keumgang Cha, Junhoon Seo, Taekyung Lee

Abstract—As the potential of foundation models in visual tasks has garnered significant attention, pretraining these models before downstream tasks has become a crucial step. The three key factors in pretraining foundation models are the pretraining method, the size of the pretraining dataset, and the number of model parameters. Recently, research in the remote sensing field has focused primarily on the pretraining method and the size of the dataset, with limited emphasis on the number of model parameters. This paper addresses this gap by examining the effect of increasing the number of model parameters on the performance of foundation models in downstream tasks such as rotated object detection and semantic segmentation. We pre-trained foundation models with varying numbers of parameters, including 86M, 605.26M, 1.3B, and 2.4B, to determine whether performance in downstream tasks improved with an increase in parameters. To the best of our knowledge, this is the first billion-scale foundation model in the remote sensing field. Furthermore, we propose an effective method for scaling up and fine-tuning a vision transformer in the remote sensing field. To evaluate general performance in downstream tasks, we employed the DOTA v2.0 and DIOR-R benchmark datasets for rotated object detection, and the Potsdam and LoveDA datasets for semantic segmentation. Experimental results demonstrated that, across all benchmark datasets and downstream tasks, the performance of the foundation models and data efficiency improved as the number of parameters increased. Moreover, our models achieve the state-of-the-art performance on several datasets including DIOR-R, Potsdam, and LoveDA.

Index Terms—Remote Sensing, Foundation Model, Scaling Vision Transformer, Pretraining, Self Supervised Learning, Masked Image Modeling, Object Detection, Semantic Segmentation.

I. INTRODUCTION

REMOTE sensing has become an essential field for various applications, and researchers have sought to address image analysis problems using deep learning methods [23]–[29]. To address remote sensing problems with deep learning applications, it is crucial to formulate the problem well in a deep learning context and obtain high-quality data. In order to create high-quality data, many remote sensing experts explore areas they want to detect or classify and collect high-quality imagery. After defining the properties of the target to detect, objects in the collected imagery are labeled, and the model is trained. However, unlike in fields dealing with natural images, this process is challenging in remote sensing. Firstly, some objects of interest appeared too rarely to be detected, and the number of times they are exposed and remotely detected is minimal. As a result, in order to collect imagery, it is necessary to know in advance the time and place where the objects

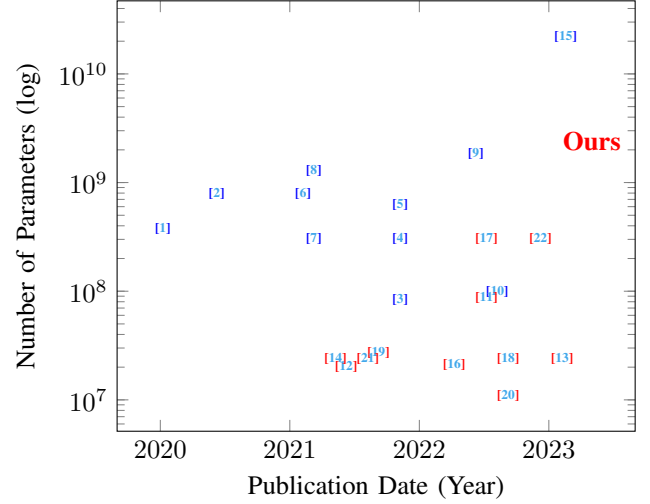


Fig. 1. The given figure shows the variation in the size of foundation models over the years, with blue and red representing the number of parameters in computer vision and remote sensing models, respectively. While the billion-scale foundation model is already being studied in computer vision, it has not yet been developed in remote sensing. More detailed information can be found Table I.

appear, which is nearly impossible. Secondly, many remote sensing experts are needed to obtain imagery and label data in a short time, making the time required to create a deep learning model comparatively longer than in other fields.

Due to the limited amount of accessible data with label compared to other fields, many studies have used fine-tuning methods with backbones trained on large amounts of data from natural images such as ImageNet, known for its ability to extract good representations [30]–[33]. However, since models pretrained with natural images such as ImageNet have a domain gap with remote sensing imagery, a large amount of high-quality labeled data is still required to make sufficient performance. Although models with enough labeled data demonstrate performance meeting requirements, they cannot approach multiple problems, a chronic issue of supervised learning. Consequently, addressing just one problem requires significant expenditure of economic and time resources.

To tackle this issue, foundation models have been proposed in the computer vision field. Foundation models can be obtained by training a model with many parameters using unlabeled images or multiple modalities that describe a single situation. This is also called pretraining, and through this process, the foundation model can extract representations without label [34]–[36]. When fine-tuning with the foundation model as an initial point, remarkable results are achieved. In simple tasks

Manuscript received. (Corresponding author: Keumgang Cha)

The authors are with SI Analytics, Daejeon 34051, South Korea (e-mail: chagmgang@si-analytics.ai; jhseo@si-analytics.ai; greatlight@si-analytics.ai).

TABLE I

THE DETAILED INFORMATION OF THE MODELS INDICATED **FIGURE 1**. WITH THE EXCEPTION OF THE MODEL INTRODUCED IN THIS PAPER, THE REMOTE SENSING MODELS ARE HANDLED WITH THE MILLION-SCALE, WHILE COMPUTER VISION HAS ALREADY SURPASSED THE BILLION-SCALE IN RECENT MODELS.

Field	Referred as	Model Name	# of Parameters
CV	BYOL [1]	ResNet200 2x	375 Million
	SimCLR v2 [2]	ResNet152 3x w sk	795 Million
	DINO [3]	ViT Base	84 Million
	iBOT [4]	ViT Large	307 Million
	MAE [5]	ViT Huge	632 Million
	ALIGN [6]	EfficientNet-L2	800 Million
	CLIP [7]	ViT Large	307 Million
	SEER [8]	RegNety-256gf	1.3 Billion
	Scaling ViT [9]	ViT Giant/14	1.8 Billion
	22B ViT [15]	ViT 22B	22 Billion
RS	Advanced [10]	ViTAE-Base	89 Million
	RingMo [11]	Swin Base	88 Million
	Geograph [12]	ResNet50	24 Million
	SSL in Domain [13]	ResNet50	24 Million
	SeCo [14]	ResNet50	24 Million
	JointSAREO [16]	ViT Small	21 Million
	SatMAE [17]	ViT Large	307 Million
	MM Contrastive [18]	ResNet50	24 Million
	SAR-EO [19]	ResNet50	25 Million
	Image-text [20]	ResNet18	11 Million
	Image-audio [21]	ResNet50	24 Million
	Scale-MAE [22]	ViT Large	307 Million
	Ours	ViT G12 \times 4	2.4 Billion

like object classification, fine-tuning the foundation model with only a few labeled data can yield higher performance than training with all labeled data and a basic model [1], [37]–[39]. Because the property of the pretraining data is in-domain, it can result in higher performance in various tasks than pretraining on natural images and fine-tuning [16], [18], [40], [41]. Moreover, as the number of parameters constituting the model increases, performance improves gradually during fine-tuning [8], [9], [15]. In other words, when pretraining the foundation model, the most crucial factors are the pretraining method, the amount of pretraining data, and the number of parameters constituting the model.

Following these achievements, numerous studies have been conducted on how to pretrain and create remote sensing domain-oriented foundation models. Typically, the pretraining methods for creating a foundation model in remote sensing include the following. The first is pretraining with images from a single sensor using fundamental methods such as contrastive learning [18], masked image modeling [10], [11], [22], and self-distillation [16]. The second method involves using multi-modal information represented by audio, text, and imagery in computer vision, but geo-location [12], audio [21], and multi-spectral imagery [17], [38] in remote sensing. Pretraining with multi-modal information demonstrates better performance than using a single modality.

Nonetheless, most studies related to pretraining in remote sensing have focused primarily on the size of the pretraining dataset or the learning method, making it difficult to find research results on the size of the foundation model, such as [11]. In the existing remote sensing field, foundation model research typically deals with ResNet50 (25.6M), ResNet101 (44.5M), and vision transformer Base (86M) models [42], [43].

As shown in **Figure 1**, the number of parameters in remote sensing models is considered to be relatively small compared to those in computer vision.

This paper addresses the extent of the number of model parameters, which is the last remaining element for building foundation models in remote sensing. For the first time, we deal with the billion-scale model in remote sensing, and prove the effect of increasing the size of the model from million-scale to billion-scale. In order to confirm the effect of the number of parameters of the foundation model constituting the backbone in the pretraining and fine-tuning strategy, we use the pretraining dataset and pretraining method from previous research that proposed successful foundation model construction [10]. Specifically, the dataset, pretraining method, and foundation model structure are the same as in previous research, namely MillionAID [44], MAE [5], and vision transformer [43]. The only altered variable is the number of parameters constituting the model. By transforming the model to 86M, 605.26M, 1.3B, and 2.4B, we confirm that the performance of the foundation model improves in proportion to the number of parameters. In addition, as a way to increase the number of parameters of the vision transformer for retaining the ability of object localization, it is suggested that not only the layer, hidden size, and dimension but also parallelism can be controlled. At last, the performance of the foundation model is confirmed by fine-tuning on DOTA v2.0, DIOR-R, Potsdam¹ and LoveDA datasets, representing rotated object detection and semantic segmentation [45]–[47] which require the ability of object localization.

II. RELATED WORKS

A. Self-supervised Learning in Computer Vision

In order to solve problems in mentioned **section I**, a lot of research has been studied on pretraining methodologies that create foundation models that can obtain good representations using unlabeled images in computer vision field [48], [49]. As shown in **Figure 2**, the methodology of pretraining using only unlabeled images can be introduced into three major methods.

The first is the contrastive learning methodology, which shows that unlabeled images can be utilized as input for the first time in the area of computer vision pretraining [37], [50].

In simple terms, the contrastive learning is to learn whether a pair of images is similar or different. The similar pairs are created by applying different transformations from one image, and different pairs are created by applying transformations to different images. In contrastive learning, the similar pairs are called positive pairs, and the different pairs are called negative pairs. After obtaining the positive and negative pairs, using the InfoNCE loss [51], the model is trained to minimize the distance between positive pairs, and maximize the distance between negative pairs.

The second is self-distillation. The self-distillation is learning to predict relationships between multiple views of an unlabeled image. The method for generating multiple views of image is similar to the approach used in contrastive learning

¹<https://www.isprs.org/education/benchmarks/UrbanSemLab/2d-sem-label-potsdam.aspx>

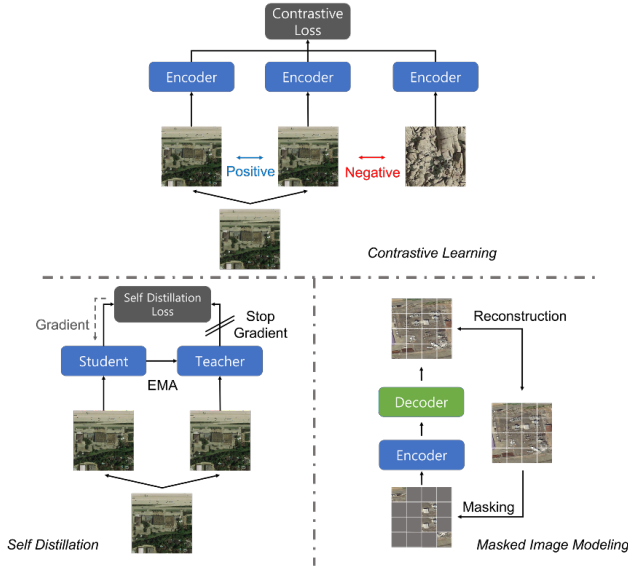


Fig. 2. A brief introduction of self supervised learning, such as contrastive learning, self-distillation and masked image modeling in computer vision. In contrastive learning, the positive pairs of data are brought closer together while the negative pairs are pushed further apart. Self-distillation is a process of training a model to predict the relationships between multiple views of an unlabeled image. Masked image modeling involves masking a portion of an image and then using a process to reconstruct the masked section.

for creating positive pairs. The one of multiple views is the input image of the **student** model and the different one of multiple views are regarded as the input of **teacher** model. And each representation is adjusted to be located at a similar point using MSE [1], InfoNCE [52], or knowledge distillation loss [3], [4]. What is important in this method is that the weight of **teacher** model is not updated by backpropagation, but by exponential moving average of the **student** model.

At last, the masked image modeling is introduced. The masked image modeling randomly masks parts of an image and learns to reconstruct the masked part [5], [53]. There are several methods for masking image modeling, but there are two most representative methods. The one is to predict the pixel values of the masked area by MSE loss [5]. The other is predicting tokenized image patches through cross entropy loss [54], [55].

B. Self-supervised Learning in Remote Sensing

Research on self-supervised learning has demonstrated that models trained using extensive and varied datasets offer two significant benefits: enhanced robustness and improved performance across different tasks. Specifically, parameters trained on large-scale datasets provide a good starting point, allowing models to converge more quickly and achieve better performance on various downstream tasks, such as object classification, detection, and semantic segmentation, compared to models trained from scratch. Additionally, rich feature learning is performed through pretraining with large-scale datasets, preventing overfitting on downstream tasks [56].

However, in the field of remote sensing, a wide variety of materials can be used for self-supervised learning, and it is

crucial to utilize them appropriately [57]. After determining the features to be learned, researchers must carefully select the appropriate methodology and dataset. The following introduces various self-supervised feature learning methods and datasets used in the remote sensing field [58].

1) *Single-modal contrastive learning*: Single-modal learning refers to the use of only one signal when constructing positive and negative pairs in feature learning. Single-modal contrastive learning signals can be categorized into two types based on the methods used to create positive and negative samples: instance-level and time-series-level signals.

Instance-level contrastive learning represents a common self-supervised learning technique in the remote sensing domain. This approach treats distinct augmented perspectives of identical images as positive pairs, whereas perspectives of unrelated images are deemed negative pairs [2], [59]. Within the realm of remote sensing, single-modal contrastive learning predominantly utilizes optical images through the application of the SimCLR methodology [39], [60], [61].

Time-series-level contrastive learning focuses on feature learning for temporal robustness in the remote sensing field [12], [14]. In this method, a pair for contrastive learning must be robustly generated with respect to time, and spatially identical yet temporally different pairs are regarded as positive pairs. This method is designed to handle spatial information sensitively, resulting in better performance in change detection. The Functional Map of the World (fMoW) dataset, which contains spatially identical and temporally different samples, is mainly used for this method [62].

2) *Multi-modal contrastive learning*: Various methods exist for obtaining multi-modal data for a specific scene or area. In remote sensing, multi-modal data includes not only optical imagery, text, and audio but also various sensor information, such as synthetic aperture radar (SAR) and near-infrared (NIR). Multi-modal contrastive learning aims to obtain rich feature representations through contrastive learning using these modalities.

Multi-sensor contrastive learning involves using multi-sensor images for contrastive learning to transfer information between different modalities. SAR-optical contrastive learning, which employs the most commonly used sensor data in remote sensing, is one important multi-sensor contrastive learning approach. SAR imagery is less affected by weather and lighting conditions than optical imagery, leading to an increase in studies using SAR imagery. However, SAR imagery is difficult to interpret even for remote sensing experts. Consequently, optical images are often used to aid in the interpretation of SAR imagery. Both optical and SAR images are used to create rich representations [18], [19], [63], [64]. For this method, a pair of spatially identical SAR and optical images is required. The SSL4EO-S12 dataset is suitable for SAR-optical contrastive learning, providing not only multi-modal data corresponding to SAR-optical but also multi-sensor images obtainable from Sentinel 1 and 2 [65]–[67]. Additionally, the QXS-SAROPT dataset can be used for SAR-optical contrastive learning [68]. This dataset includes relatively high-resolution images compared to SSL4EO-S12.

Image-text contrastive learning is the most widely used

approach related to multi-modality in the computer vision field [6], [7]. However, generating text corresponding to an image in remote sensing is more difficult compared to the computer vision field, where text is readily available on the web. As a result, it is challenging to find studies that apply image-text contrastive learning methods in remote sensing. Only one work related to image-text contrastive learning has been found [20], which uses the RSICD [69] and UCM [70] datasets.

Image-audio contrastive learning is also rare for the same reasons as image-text, but one study has been found [21]. This study created a dataset called SoundingEarth, comprising 50,545 pairs of remote sensing image-audio samples. They collected audio recordings from various locations such as residential areas, parks, lakes, and wilderness scenes, with corresponding high-resolution RSIs obtained from Google Earth. Using SoundingEarth, the authors employed a technique similar to image-text multi-modal contrastive learning.

3) *Self-distillation learning*: can be considered a form of contrastive learning, but its main distinction is that it does not use negative pairs. Many studies focus on learning single-modal features [71]. However, further attempts are being made to learn multi-sensor and temporal information [16], [72], [73].

4) *Generative learning*: The primary goal of generative learning is to train a model to reconstruct an original input even when it is partially corrupted. In general computer vision, removing spatial and temporal information from the original input is employed. Similarly, a comparable method is used in the field of remote sensing.

Generation from missing spatial information involves learning features by reconstructing the corrupted area of the original image using the characteristics of the surrounding space. Generative adversarial networks (GANs) [74] and reconstruction with auto-encoding are primarily used for representation learning. In MARTA GANs [75], which is related to generative adversarial networks, the discriminator serves as the encoder for the scene classification model. On the other hand, numerous studies focus on reconstruction with auto-encoding [10], [11], [76]. The auto-encoding method primarily employs a corrupted image as input with an encoder-decoder structure model using L1 or L2 distance metrics. Additionally, a study on reconstruction by reflecting the characteristics of ground sample distance (GSD), an essential feature in remote sensing images, has been conducted [22].

Generation from missing temporal information is similar to video frame prediction in the computer vision field. By recovering the missing temporal information of the input image, such as frame prediction, the encoder model is trained to extract good representations [17], [77], [78]. Like time-series-level contrastive learning, this method requires datasets containing images taken of the same place at different times. Therefore, the fMoW dataset is commonly used for this approach [62].

C. Foundation Models in Computer Vision Field

Until recently, deep learning research has primarily focused on creating task-specific models and securing good performance. However, creating a task-specific model involves

considerable time and cost for collecting, labeling, and training a model suitable for the task. The latest trend in deep learning is to use foundation models, which can replace task-specific models. These models are pretrained on vast amounts of unlabeled data and can be fine-tuned to various tasks. Since the foundation model is already pre-learned using a substantial amount of data, it is trained to extract representations effectively. As a result, the cost required to create a task-specific model through the foundation model is much lower than that of previous methodologies. While foundation models related to natural language processing are widely created and studied [79], [80], foundation models addressing computer vision problems are just being investigated [81].

The three most important factors in creating a foundation model are a large-scale dataset, a large-scale model, and a pretraining method. In the computer vision field, large-scale datasets have already been constructed with single-modal and multi-modal data, such as ImageNet [82], JFT-300M [83], LVIS [84], and LAION-400M [85]. The second factor is the large-scale model. Following the 175B-parameter model already established in natural language processing, efforts are being made to gradually increase the number of parameters in computer vision models. Using vision transformers or RegNet, researchers have successfully built models with 1.3B [8], 2B [9], and 22B parameters [15], demonstrating better performance than most previous models. Finally, the methodology for learning foundation models varies greatly depending on the dataset used. For instance, single-modal learning employs SimCLR [2], [37], BYOL [1], DINO [3], and iBOT [4], while multi-modal learning uses CLIP [7], BEiT-3 [86], and UniPerceiver [87].

As the foundation models become more prevalent in computer vision, their applicability to remote sensing tasks is expected to grow. By leveraging these pre-trained models, researchers and practitioners can reduce the time and effort required to develop task-specific models in the remote sensing field. Moreover, these foundation models can potentially lead to better representations and improved performance across various remote sensing tasks, including object detection, change detection, and semantic segmentation.

III. METHODS

In this section, we discuss the details of the model architecture (vision transformer) [43], pretraining dataset (Million-AID) [44], and pretraining method (MAE) [5]. Additionally, we explain how to properly scale up the vision transformer, which is one of the essential contributions of this work [88]. Furthermore, we address how to adapt the plain vision transformer for tasks like rotated object detection and semantic segmentation, which require high-resolution input imagery and object localization ability [89].

A. Self Supervised Learning by MAE

To demonstrate that the performance of the foundation model improves with the increase in the number of model parameters when pretrained using the same number of datasets in the remote sensing field, we pretrain models with different

numbers of parameters using MAE [5] and the large-scale remote sensing imagery dataset, MillionAID [44].

1) *MillionAID*: The MillionAID dataset [44] is easily accessible and contains the largest number of RGB images. This dataset is designed for scene classification tasks and includes approximately 1,000,848 non-overlapping remote sensing scenes. It features 51 detailed classes, organized in a three-level tree structure. The 51 individual components (leaf nodes) are assembled into 28 broader categories (parent nodes) at the secondary tier, which are subsequently classified into eight principal clusters (nodes) at the primary level. These dominant clusters embody diverse land use classifications, including agricultural, industrial, public amenities, and residential zones. To build a robust model at varying ground sample distances (GSD), the images are collected from Google Earth, with resolutions ranging from 0.5m to 153m per pixel. The images also vary in size, from 110×110 to $31,672 \times 31,672$ pixels. While each image is mapped to a class, these images are considered unlabeled data, so only the images are used for pretraining. Although it is evident that more pretraining images lead to better foundation model performance, this paper focuses on the effect of the number of model parameters during training, using only MillionAID for a fair comparison with other research [10].

2) *MAE*: MAE [5] learns representations by reconstructing randomly masked images using the encoder-decoder structure of the vision transformer. Images are divided into non-overlapping patches of fixed size and tokenized by projecting them into a patch embedding layer. After projection, 75% of the projected patches are dropped in a masking process, and only the remaining 25% of visible patches are fed into the encoder. Then, learnable tokens representing the masked patches and the encoded features are combined and passed to the decoder. Finally, the features passed through the decoder are projected to reconstruct the masked area of the original image. During training, the model is optimized to reduce the distance between the pixel values of the output and the original image. The loss calculation includes only the masked area, excluding the visible patch area.

3) *Scaling Up Vision Transformer*: While several rules exist for scaling up the transformer structure in natural language processing, which heavily relies on transformer structures [90], [91], these rules may not be as effective for scaling up vision transformers. For instance, in most self-supervised learning papers using vision transformers in computer vision, only classification and semantic segmentation performance are introduced, and it is challenging to find object detection performance [3], [5], [55], [92]. If object detection performance is presented, the research typically involves a model with a significantly smaller number of parameters [4]. As shown in Figure 3, a study connects the multi-head self-attention structure and feed-forward blocks in parallel, which has a similar effect as stacking them serially [88]. Based on this approach, this paper demonstrates that object detection and semantic segmentation, which are crucial downstream tasks in remote sensing, can be performed effectively by scaling up the vision transformer in parallel.

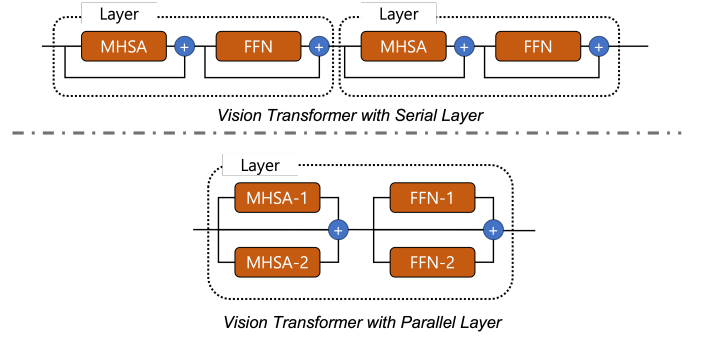


Fig. 3. This figure explains how to effectively increase the number of parameters of the vision transformer, and the two models have substantially the same amount of computation and number of parameters. In the field of natural language processing, multi head self attention and feed forward blocks are configured only serially, but there is the difference of performance even if they are configured in parallel. Like 12 layers with 1 parallelism and 6 layers with 2 parallelism, if the same number is obtained when multiplying the layer and parallelism, the backbone has the same number of parameters and the same flops.

4) *Implementation Detail for Pretraining*: This paper primarily focuses on analyzing the scaling up of the model. Therefore, the configuration of the models used in this study is introduced first. The detailed information of the vision transformer for the experiment is shown in Table II. In order to scale up the vision transformer effectively, the number of parallelism, hidden size, MLP size, and heads are changed, while the number of layers is fixed at 12. The method of naming the model is as follows. The model name is follows ViT-(A)(B) \times (C). (A), (B) and (C) stand for hidden size, layers and parallelism, respectively. For example, ViT-G12 \times 4 has the 2048 hidden size, 12 layers, and 4 parallelism. In case of ViT-B12 \times 1, this model has same structure of standard vision transformer base. During pretraining, input images are resized and cropped to 224×224 using random resized crop transformation². After resizing and random cropping, horizontal flip and vertical flip are sequentially applied with a 50% probability. The input image is then divided into 16×16 patches before being fed into the vision transformer encoder, resulting in $(224/16) \times (224/16)$ sampled patches. In the original MAE, pretraining is applied with 1600 epochs [5]. However, since models with a large number of parameters can experience overfitting to the pretext task (MAE in this paper), the models are pretrained with 400 epochs using the AdamW optimizer [95] and a batch size of 2048. In general, the learning rate should be different according to the batch size even in the same experiment. Since it is not appropriate for expressing the hyper parameters, the learning rate is expressed with the value of base learning rate. The effective learning rate is as follows, $batchsize \times BaseLR/256$. It is worth noting that only the ViT-G12 \times 4 model has a different base learning rate than the other models. This is because the loss did not converge when a learning rate of $1.5e^{-4}$ was applied, but it did converge when $1e^{-4}$ was used. For the mask portion, the same 75% value is used as in previous research [10]. Additionally,

²<https://pytorch.org/vision/main/generated/torchvision.transforms.RandomResizedCrop.html>

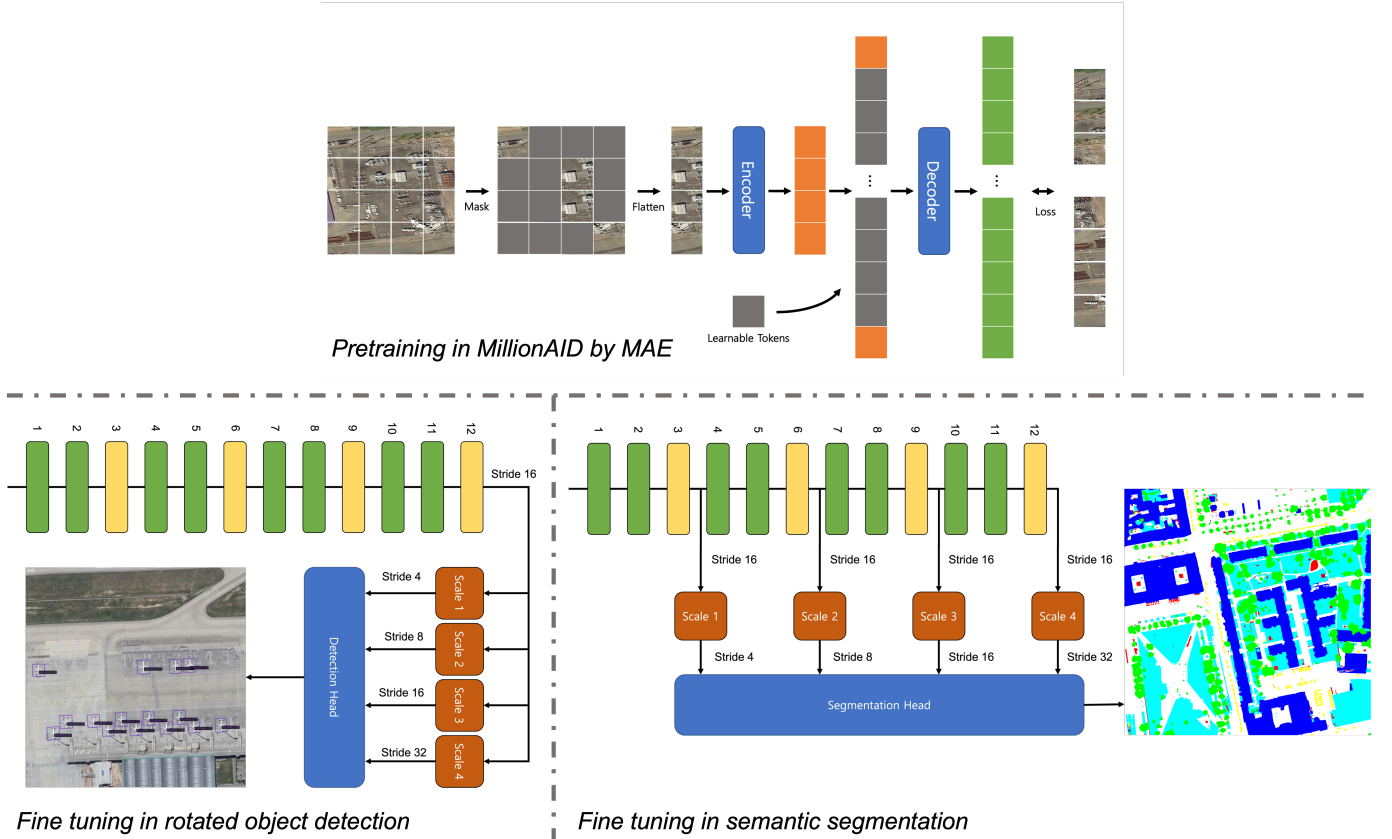


Fig. 4. This figure shows overall flows for pretraining and downstream tasks. The plain vision transformer is pretrained by MAE with remote sensing imagery dataset, MillionAID. Then, plain vision transformer is converted to ViTDE structure with local and global attention for downstream tasks which is rotated object detection and semantic segmentation. In order to upsample and downsample features, scale blocks are adopted after ViTDE backbone. The scale block 1 consists of serially connected transposed convolution, normalization, GELU, and transposed convolution [93], [94]. The scale block 2 is only transposed convolution. The scale block 3 is identity block. The scale block 4 is max pooling with kernel size 2. All transposed convolutions used in scale block is with kernel size 2 and stride size 2.

TABLE II
THE CONFIGURATION OF MODELS HANDED IN THIS RESEARCH.

Name	Hidden size	MLP size	Heads	Params
ViT-B12×1 [10]	768	3072	12	86M
ViT-L12×4	1024	4096	16	605.26M
ViT-H12×4	1536	6144	16	1.36B
ViT-G12×4	2048	8192	32	2.42B

TABLE III
THE HYPER PARAMETER OF PRETRAINING.

Name	Epochs	Base LR	Weight Decay
ViT-B12×1 [10]	1600	0.00015	0.05
ViT-L12×4	400	0.00015	0.05
ViT-H12×4	400	0.00015	0.05
ViT-G12×4	400	0.0001	0.05

due to the large size of the model presented in this paper, activation checkpointing and fp16 were applied for pretraining to address the issue of insufficient GPU memory [96].

B. Fine Tuning Vision Transformer for Object Localization

Downstream tasks such as rotated object detection and semantic segmentation require the ability to localize objects and high-resolution input images, e.g., 1024×1024 . However,

the pretrained backbone has a plain and non-hierarchical structure, which calculates the relationship between all patches. Consequently, it is not suitable to use without transformation in terms of operation speed and GPU memory. To address this problem, local and global attention introduced in ViTDE [89] is applied, which can reduce computation and GPU memory usage without degrading performance. As shown in Figure 4, local attention with a window size of 14 is applied to blocks 1, 2, 4, 5, 7, 8, 10, and 11, while global attention is applied to blocks 3, 6, 9, and 12. In rotated object detection tasks, the feature of the last layer is resampled to have a ratio of 4, 2, 1, 0.5 through each scale block, known as a simple pyramid network [89]. In semantic segmentation, the features of layers 3, 6, 9, and 12 are resampled to have ratios of 4, 2, 1, and 0.5 through each scale block, respectively. These features are then fed into the detection head and segmentation head.

IV. EXPERIMENTAL RESULTS

In this section, we evaluate the performance of the proposed models on remote sensing downstream tasks, including rotated object detection and semantic segmentation, after pretraining. We then examine whether the performance increases in proportion to the number of parameters of the pretrained model across all datasets and benchmarks. We compare the

performance with other studies, but the comparison group pretrained in remote sensing mainly includes the previous studies [10]. This is because the amount of pretraining data (MillionAID) and the methodology used in pretraining (MAE) should be the same for fair comparison.

To demonstrate whether the ability to extract representations increases as the number of parameters included in the model increases, we conduct sample efficiency experiments with DIOR-R for rotated object detection and Potsdam for semantic segmentation. To obtain sample efficiency results, we use 1%, 5%, 10%, 50%, and 100% of the training dataset and 100% of the test dataset for evaluation.

A. Rotated Object Detection

1) *Dataset*: In this paper, two benchmark dataset is adopted to evaluate the performance of pretrained models: DOTA v2.0 [45] and DIOR-R [46].

DOTA v2.0. The DOTA dataset is the most well-known dataset as a benchmark for rotated object detection in the remote sensing field. We use DOTA v2.0 for evaluation because of its better integrity than v1.0. To make the model robust at various resolutions, images are collected from multiple sources and consist of images with pixel ranges from 800×800 to $20,000 \times 20,000$. DOTA v2.0 has 18 categories including harbor, swimming-pool, roundabout, bridge, baseball-diamond, ground-track-field, soccer-ball-field, storage-tank, basketball-court, large-vehicle, plane, tennis-court, ship, helicopter, helipad, container-crane, airport, and small-vehicle. Also, it has 11,268 images and 1,793,658 instances. The training dataset contains 1,830 images and 268,627 instances. The validation dataset contains 593 images and 81,048 instances. And, the test-dev contains 2,792 images and 353,346 instances. However, the test-dev is published with only images. The test-challenge dataset contains 6,053 images and 1,090,637 instances. However, because the test-challenge dataset is only published during challenge, it can not be accessible now. We evaluate our model by submitting the inference result to the server³.

DIOR-R. The DIOR-R dataset is also widely used as a benchmark for evaluating rotated object detection performance in remote sensing. The DIOR-R dataset is divided into training, validation and test. It has 20 categories including expressway-toll-station, chimney, baseball-field, vehicle, harbor, basketball-court, golf-field, tennis-court, storage-tank, windmill, train-station, bridge, ground-track-field, ship, airport, airplane, Expressway-Service-area, dam, stadium, and overpass. It includes 11,738 images and 68,073 instances by bundling training with validation. The test contains 11,738 images and consists of 124,445 instances. All images are 800×800 in size, pixel resolution is from 0.5m to 30m. Unlike DOTA v2.0, the training, validation and test datasets are totally published with both images and instances. We evaluate our model locally using the published dataset.

2) *Implementation Details and Experiment Settings*: As in other research, we train the rotated object detection models with the same hyperparameters, regardless of the dataset, and

only change the pretrained backbone. The detection models are trained based on the mmrotate framework⁴ with added dataset functionality [97]. We use the AdamW optimizer [95], with a learning rate of 0.0001 and weight decay of 0.05. The training schedule is designed for a batch size of 2 and 12 epochs, with the learning rate being reduced by $10\times$ at the 8th and 11th epochs. We also apply a 0.8 layer-wise learning rate decay strategy and a drop path rate of 0.1 to ViTDET.

We select and fix the roi transformer [98] as the detection head, which has the best performance in the mmrotate framework. Since [10] has evaluated the performance with Oriented R-CNN [99] but not on the DOTA v2.0 dataset, we re-implement and evaluate the detection model composed of the backbone weight published by [10] and the roi transformer. The backbone is converted into the ViTDET architecture, as shown in subsection III-B.

Due to the wide range of pixel sizes in the DOTA v2.0 dataset, we crop each image to a size of 1024×1024 with a stride of 824. For the DIOR-R dataset, images are already set to a constant size of 800×800 , so cropping is not performed. During training, we use only random horizontal and vertical flips as data augmentation for both datasets. Test-time augmentation is not applied during inference on test images, and models are evaluated based on average precision (AP) for each category and mean average precision (mAP), which is the average of APs across all categories.

3) *Experiment Results*: Table IV and Table V show the performance results for DOTA v2.0 and DIOR-R, while Table VI displays the results of sample efficiency experiments using different amounts of training data. In the tables, red and blue text represent the highest and second-highest performance, respectively. Specifically, the smaller datasets are obtained by randomly sampling 1%, 5%, 10%, 50%, and 100% of the images. The number of objects included in each dataset can be seen in Table VII.

DOTA v2.0. Table IV displays the performance results for various models, including our experiments. The results for models other than ours are taken from the official paper [45]. As noted in the caption of Table IV, the † represents the result of metrics using the mmrotate framework for fair evaluation. The abbreviations of method are: Mask R-CNN (MR) [101], CMR-Cascade Mask R-CNN (CMR) [102], Hybrid Task Cascade without a semanticbranch (HTC) [102], Faster R-CNN(FR) [103], Deformable Roi Pooling (Dp) [104] and RoI Transformer (RT) [98]. The short names for categories are defined as: PL (Plane), BD (Baseball diamond), BR (Bridge), GTF (Ground track field), SV (Small-vehicle), LV (Large-vehicle), SH (Ship), TC (Tennis-court), BC (Basketball-court), ST (Storage-tank), SBF (Soccer-ball field), RA (Roundabout), HA (Harbor), SP (Swimming-pool), HC (Helicopter), CC (Container-crane), AP (Airport), and HL (Helipad). In backbone column, the IMP means ImageNet classification pre-training. The MAE means MAE on the MillionAID. Because existing benchmarks have not been performed on mmrotate framework, the † means the result of evaluation using RoI Transformer in Res50 with mmrotate framework. In order to

³<https://captain-whu.github.io/DOTA/evaluation.html>

⁴<https://github.com/open-mmlab/mmdetection>

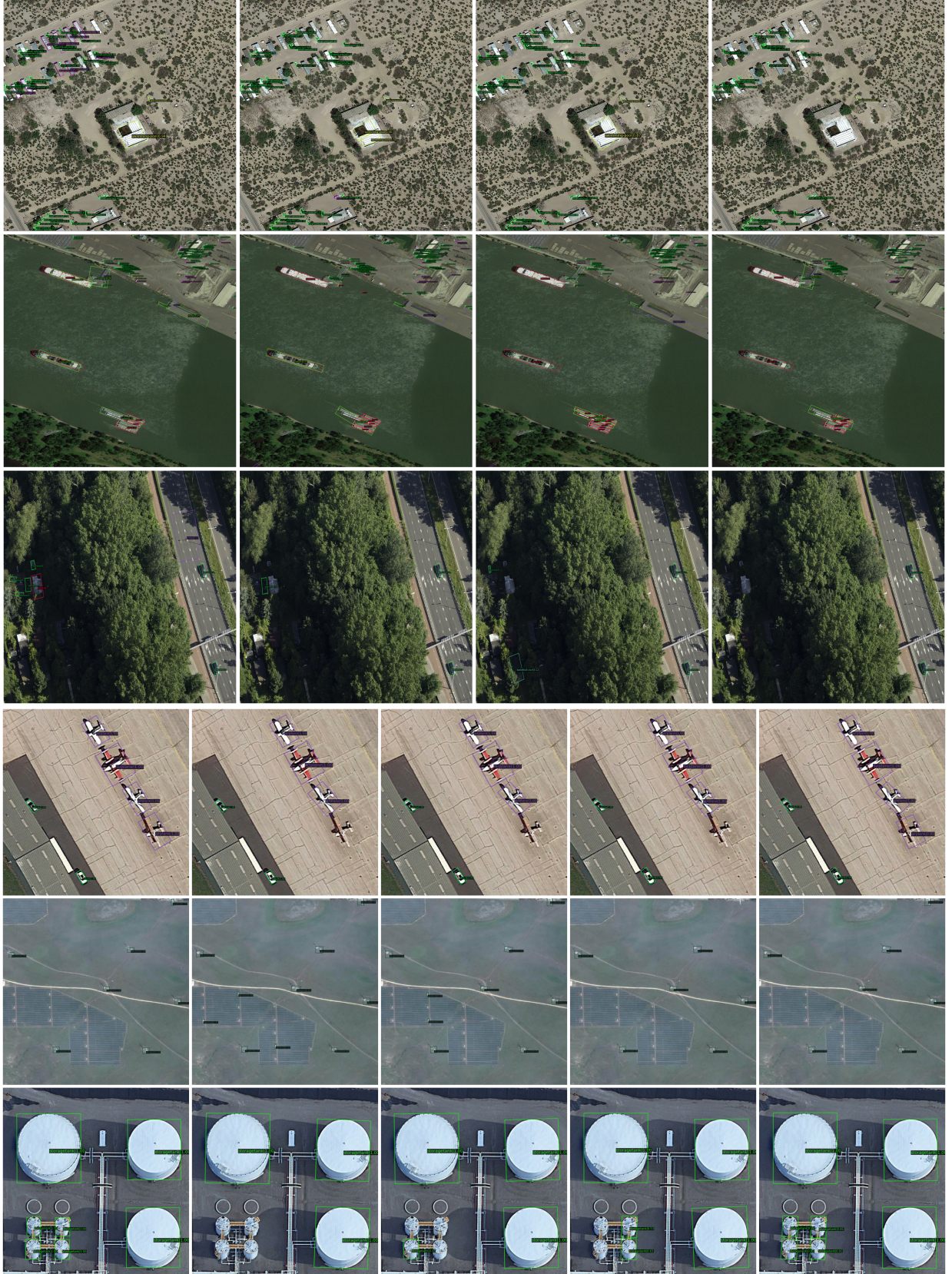


Fig. 5. Visualization results of the proposed model. The first through third rows are the results of the DOTA v2.0 dataset. Since the label of test dataset in DOTA v2.0 is unavailable, the images from left to right are ViT-B12 \times 1, ViT-L12 \times 4, ViT-H12 \times 4, and ViT-G12 \times 4. The fourth to sixth rows are the results of the DIOR-R dataset. The images from left to right are label, ViT-B12 \times 1, ViT-L12 \times 4, ViT-H12 \times 4, and ViT-G12 \times 4.

TABLE IV

THE RESULTS OF CLASS-WISE AP AND MAP ON DOTA V2.0. BECAUSE EXISTING BENCHMARKS HAVE NOT BEEN PERFORMED ON MMROTATE FRAMEWORK, THE † MEANS THE RESULT OF EVALUATION USING ROI TRANSFORMER IN RES50 WITH MMROTATE FRAMEWORK. ◇ IS THE RESULT RE-IMPLEMENTED IN MMROTATE FRAMEWORK USING THE VISION TRANSFORMER WEIGHT PUBLISHED BY [10] WITH ROI TRANSFORMER.

Backbone	Method	PL	BD	BR	GTF	SV	LV	SH	TC	BC	ST	SBF	RA	HA	SP	HC	CC	AP	HL	mAP
Res50(IMP) [42]	RetinaNet [100]	70.63	47.26	39.12	55.02	38.1	40.52	47.16	77.74	56.86	52.12	37.22	51.75	44.15	53.19	51.06	6.58	64.28	7.45	46.68
Res50(IMP) [42]	MR [101]	76.2	49.91	41.61	60	41.08	50.77	56.24	78.01	55.85	57.48	36.62	51.67	47.39	55.79	59.06	3.64	60.26	8.95	49.47
Res50(IMP) [42]	CMR [102]	77.01	47.54	41.79	58.2	41.58	51.74	57.86	78.2	56.75	58.5	37.89	51.23	49.38	55.98	54.59	12.31	67.33	3.01	50.04
Res50(IMP) [42]	HTC [102]	77.69	47.25	41.15	60.71	41.77	52.79	58.87	78.74	55.22	58.49	38.57	52.48	49.58	56.18	54.09	4.2	66.38	11.92	50.34
Res50(IMP) [42]	FR OBB [103]	71.61	47.2	39.28	58.7	35.55	48.88	51.51	78.97	58.36	58.55	36.11	51.73	43.57	55.33	57.07	3.51	52.94	2.79	47.31
Res50(IMP) [42]	FR OBB + Dp [104]	71.55	49.74	40.34	60.4	40.74	50.67	56.58	79.03	58.22	58.24	34.73	51.95	44.33	55.1	53.14	7.21	59.53	6.38	48.77
Res50(IMP) [42]	FR H-OBB [103]	71.39	47.59	39.82	59.01	41.51	49.88	57.17	78.36	56.87	58.24	37.66	51.86	44.61	55.49	54.74	7.56	61.88	6.6	48.9
Res50(IMP) [42]	FROBB + RT [98]	71.81	48.39	45.88	64.02	42.09	54.39	59.92	82.7	63.29	58.71	41.04	52.82	53.32	56.18	57.94	25.71	63.72	8.7	52.81
Res50(IMP)† [42]	FROBB + RT [98]	77.84	51.54	45.97	65.78	43.25	55.03	60.38	79.45	62.98	59.85	46.89	56.53	54.06	56.71	51.65	21.31	68.05	8.32	53.64
ViT-B12×1(MAE)◇ [10]	FROBB + RT [98]	79.49	55.86	50.12	65.36	43.82	56.63	61.18	79.07	62.24	60.62	41.71	57.88	58.48	64.84	58.83	35.13	89.41	14.14	57.49
ViT-L12×4(MAE)(Ours)	FROBB + RT [98]	79.75	53.34	49.02	65.18	43.8	56.83	61.28	83.08	60.77	66.83	42.33	58.33	57.39	64.84	67.31	30.81	80.69	13.8	57.52
ViT-H12×4(MAE)(Ours)	FROBB + RT [98]	79.8	53.26	49.32	64.28	43.9	56.46	61.18	78.98	63.53	60.71	42.76	57.74	57.84	64.43	67.34	34.69	89.35	14.3	57.77
ViT-G12×4(MAE)(Ours)	FROBB + RT [98]	80.12	54.12	50.07	65.68	43.98	60.07	67.85	79.11	64.38	60.56	45.98	58.26	58.31	64.82	69.84	32.78	89.37	11.07	58.69

TABLE V

THE RESULTS OF CLASS-WISE AP AND MAP ON DIOR-R. AS SAME WITH TABLE IV, ◇ IS THE RESULT RE-IMPLEMENTED IN MMROTATE FRAMEWORK USING THE VISION TRANSFORMER WEIGHT PUBLISHED BY [10] WITH ROI TRANSFORMER.

Backbone	Method	APL	APO	BF	BC	BR	CH	DAM	ETS	ESA	GF	GTF	HA	OP	SH	STA	STO	TC	TS	VE	WM	mAP
Res50(IMP) [42]	RetinaNet [100]	61.49	28.52	73.57	81.17	23.98	72.54	19.94	72.39	58.2	69.25	79.54	32.14	44.87	77.71	67.57	61.09	81.46	47.33	38.01	60.24	57.55
Res50(IMP) [42]	FR OBB [103]	62.79	26.8	71.72	80.91	34.2	72.57	18.95	66.45	65.75	66.63	79.24	34.95	48.79	81.14	64.34	71.21	81.44	47.31	50.46	65.21	59.54
Res50(IMP) [42]	FROBB + RT [98]	63.34	37.88	71.78	87.53	40.68	72.6	26.86	78.71	68.09	68.96	82.24	47.71	55.61	81.21	78.23	70.26	81.61	54.86	43.27	65.52	63.87
Res50(IMP) [42]	Gliding Vertex [105]	65.35	28.87	74.96	81.33	33.88	74.31	19.58	70.72	64.7	72.3	78.68	37.22	49.64	80.22	69.26	61.13	81.49	44.76	47.71	65.04	60.06
Res50(IMP) [42]	AOPG [46]	62.39	37.79	71.62	87.63	40.9	72.47	31.08	65.42	77.99	73.2	81.94	42.32	54.45	81.17	72.69	71.31	81.49	60.04	52.38	69.99	64.41
Res50(IMP) [42]	DODet [106]	63.4	43.35	72.11	81.32	43.12	72.59	33.32	78.77	70.84	74.15	75.47	48	59.31	85.41	74.04	71.56	81.52	55.47	51.86	66.4	65.1
ViT-B12×1(MAE)◇ [10]	Oriented R-CNN [99]	81.04	41.86	80.79	81.39	44.83	78.35	35.12	67.67	84.85	75.44	80.8	37.65	59.33	81.15	78.7	62.87	89.83	56.17	49.87	65.36	66.65
ViTAE-B(MAE) [10]	Oriented R-CNN [99]	81.3	46.73	81.09	87.62	47.38	79.79	31.99	69.72	86.71	76.23	82.13	42.47	60.45	81.2	80.11	62.75	89.75	64.56	50.77	65.33	68.4
ViT-B + VSA(MAE) [10]	Oriented R-CNN [99]	81.2	50.68	80.95	87.41	51.27	80.87	34.61	76.4	88.32	78.21	83.31	45.84	64.02	81.23	82.87	71.31	89.86	64.66	50.74	65.81	70.48
ViTAE-B + VSA(MAE) [10]	Oriented R-CNN [99]	81.26	52.26	81.1	88.47	51.35	80.18	37.4	75.29	88.92	77.52	84.33	47.31	63.73	81.18	83.03	71.13	90.04	65.01	50.81	65.82	70.81
ViT-B + RVSA(MAE) [10]	Oriented R-CNN [99]	80.92	49.88	81.05	88.52	51.52	80.17	37.87	75.96	88.83	78.46	84.01	46.53	64.18	81.21	84.04	71.34	89.99	65.41	50.53	66.49	70.85
ViTAE-B + RVSA(MAE) [10]	Oriented R-CNN [99]	81.2	54.71	81.12	88.13	51.83	79.93	36.79	76.06	89.23	78.3	84.46	47.29	65.01	81.19	82.17	70.69	90.03	66.75	50.73	65.4	71.05
ViT-B12×1(MAE)◇ [10]	FROBB + RT [98]	72.25	53.86	80.55	81.49	45.15	79.96	31.56	71.44	85.42	78.67	83.72	47.57	59.55	81.26	84.87	71.28	81.51	64.73	49.43	66.05	68.52
ViT-L12×4(MAE)(Ours)	FROBB + RT [98]	81.2	60.47	81.01	89.97	51.76	80.46	39.98	78.75	89.12	78.77	84.06	53.85	60.93	81.24	84.4	71.77	90.15	66.22	51.46	66.59	72.11
ViT-H12×4(MAE)(Ours)	FROBB + RT [98]	81.59	55.01	80.87	88.96	54.27	80.76	40.61	79.73	89.47	79.47	83.84	55.28	65.27	89.52	84.42	71.91	90.06	65.97	51.8	74.12	73.15
ViT-G12×4(MAE)(Ours)	FROBB + RT [98]	81.41	61.73	81.17	89.86	54.12	80.84	40.35	79.42	89.08	79.3	84.51	55.83	65.61	89.59	86.16	71.52	90.11	66.29	51.88	73.67	73.62

compare the results with the RoI Transformer, ◇ is the result re-implemented in mmrotate framework using the vision transformer weight published by [10]. Clearly, models pretrained with MAE outperform those pretrained with IMP, with mAP differences ranging from 3.85 to 5.05. In terms of the models proposed in this paper, the relationship between the number of parameters and mAP is such that the mAP tends to increase as the number of parameters increases, with no other changes except for the number of parameters. Although the increase in mAP becomes smaller as the number of model parameters grows, it is evident that performance improves.

DIOR-R. Table V displays the performance results, with the results of models in the table taken from previous research [10]. The short names for categories are defined as: APL (Airplane), APO (Airport), BF (Baseball field), BC (Basketball court), BR (Bridge), CH (Chimney), DAM (Dam), ETS (Expressway-toll-station), ESA (Expressway-service-area), GF (Golf field), GTF (Ground track field), HA (Harbor), OP (Overpass), SH(Ship), STA (Stadium), STO (Storage tank), TC (Tennis court), TS (Transition), VE (Vehicle), and WM (Windmill). As same with Table IV, the IMP means ImageNet classification pretraining. The MAE means MAE on the MillionAID. Additionally, as shown in Table V, the ◇ represents the result re-implemented in the mmrotate framework using the vision transformer weight published by [10] with the RoI Transformer detection head. As expected, the performance of models pretrained with MAE is higher than those pretrained with IMP. Performance can be improved by changing the backbone structure using the RVSA [10] and ViTAE [107] modules proposed in previous studies. Observing performance changes based solely on the number of parameters in the backbone module, it is clear that mAP increases as the number

of backbone parameters grows. Although the rate of improvement in mAP becomes less significant as the number of model parameters increases, it is still evident that performance improves with a higher number of parameters.

Sample Efficiency in DIOR-R. Sample efficiency in fine-tuning is an important capability that a foundation model should have [79], [108]–[110]. In this context, we conduct experiments on the DIOR-R dataset using 1%, 5%, 10%, 50%, and 100% of the training data. Each dataset is sampled based on the ratio of images, meaning that they are not sampled precisely based on individual objects. More details about the portion of objects are shown in Table VII. To measure sample efficiency, the model changes only the backbone, like in other experiments, and a RoI Transformer is used as a detection head. As shown, the model achieves better performance as the number of parameters increases within the same sample ratio. Additionally, we can verify that using a backbone with a large number of parameters and well-prepared training can achieve comparable performance even if only half of the data is used, as seen with ViT-H12×4, ViT-G12×4 at 50%, and ViT-B12×1 at 100%.

These results demonstrate the effectiveness of the proposed models in improving the performance of rotated object detection tasks in remote sensing datasets. The experiments confirm that utilizing larger backbones with more parameters leads to better performance, even though the rate of improvement becomes less significant as the number of parameters increases. Furthermore, the experiments on sample efficiency show that well-prepared training with larger backbones can yield comparable results even when using a smaller portion of the training data, highlighting the importance of optimizing the model architecture and training strategy in order to achieve

TABLE VI

THE RESULTS OF CLASS-WISE AP AND MAP ON DIOR-R FOR EVALUATING SAMPLE EFFICIENCY. THE SHORT NAMES FOR CATEGORIES ARE DEFINED AS SAME WITH TABLE V. IN ORDER TO COMPARE THE RESULTS ACCORDING ONLY BACKBONE, THE ViT-B12×1 IS RETRAINED BY MMROTATE FRAMEWORK. THE TRAINING DATA OF DIOR-R IS RANDOMLY SAMPLED BY RATIO 0.01, 0.05, 0.1, 0.5, 1.0.

Sample ratio	Backbone	APL	APO	BF	BC	BR	CH	DAM	ETS	ESA	GF	GTF	HA	OP	SH	STA	STO	TC	TS	VE	WM	mAP
1%	ViT-B12×1 [10]	9.10	0.40	48.20	0.00	0.00	17.70	1.30	4.50	1.40	22.10	20.40	2.10	2.80	13.20	24.30	29.00	55.50	8.50	10.50	5.00	13.80
	ViT-L12×4	10.40	0.60	52.70	0.00	0.70	28.00	4.50	8.20	4.50	25.70	20.00	2.20	4.50	17.10	19.70	42.70	49.00	10.90	11.60	12.90	16.30
	ViT-H12×4	10.20	0.30	52.20	0.20	0.00	28.70	9.10	0.90	9.10	30.00	21.80	4.50	1.20	19.00	20.60	31.10	61.60	10.90	11.50	5.10	16.40
	ViT-G12×4	13.70	0.30	53.50	2.60	0.00	20.10	3.00	11.20	2.20	26.00	20.80	6.10	9.10	21.10	21.40	30.50	61.70	12.10	12.00	12.40	17.00
5%	ViT-B12×1 [10]	61.50	6.20	63.20	67.80	11.70	67.20	9.70	38.00	38.00	57.70	56.40	14.20	19.30	62.20	52.10	61.40	80.20	20.20	33.10	33.10	42.70
	ViT-L12×4	53.10	3.60	63.00	66.80	5.80	70.30	4.20	35.60	42.30	59.80	58.30	18.20	24.10	61.90	55.00	61.10	79.30	21.90	33.20	41.20	42.90
	ViT-H12×4	53.50	4.40	63.10	63.10	7.90	62.50	10.40	39.60	42.40	58.40	61.50	15.40	25.50	62.10	58.00	61.00	80.30	19.20	33.40	40.40	43.10
	ViT-G12×4	62.30	10.20	63.30	65.60	11.60	63.40	10.90	38.40	42.40	58.60	57.00	16.80	27.80	61.30	52.00	52.60	72.40	25.10	33.40	41.50	43.30
10%	ViT-B12×1 [10]	53.50	11.70	62.90	68.60	12.90	71.70	12.50	39.70	43.10	56.80	66.10	15.20	26.70	71.30	53.20	59.60	78.80	29.30	33.10	42.90	45.50
	ViT-L12×4	63.10	10.70	70.20	79.70	19.80	71.80	11.50	47.60	52.00	59.20	68.20	25.50	38.40	79.10	63.70	61.40	81.40	32.30	39.80	51.80	51.40
	ViT-H12×4	71.40	15.10	71.00	79.10	22.00	71.60	15.20	49.20	51.10	65.90	68.70	26.60	36.90	79.10	62.90	61.60	81.30	39.40	41.10	52.50	53.10
	ViT-G12×4	71.90	15.30	71.60	77.70	23.70	72.10	15.70	50.80	52.30	64.70	70.00	29.30	42.80	79.30	63.90	61.70	81.00	42.20	41.00	53.00	54.00
50%	ViT-B12×1 [10]	63.40	39.30	80.20	81.10	36.10	72.60	28.00	61.40	79.00	76.40	81.70	38.20	54.40	81.10	77.90	62.90	81.50	56.70	42.90	63.50	62.90
	ViT-L12×4	72.50	43.20	72.40	81.00	45.00	72.60	29.60	70.10	86.40	75.80	82.10	45.50	58.90	81.10	77.30	63.00	81.50	63.40	50.10	64.90	65.80
	ViT-H12×4	72.50	53.40	80.90	81.20	47.00	72.60	36.90	71.70	88.70	77.50	83.00	47.80	60.20	81.10	83.80	71.40	81.60	65.40	51.10	64.40	68.60
	ViT-G12×4	72.50	53.70	80.90	81.40	46.60	72.50	35.90	71.30	88.30	76.60	83.00	47.60	60.30	89.30	83.50	71.60	81.50	64.60	50.90	64.90	68.90
100%	ViT-B12×1 [10]	72.20	53.80	80.50	81.40	45.10	79.90	31.50	71.40	85.40	78.60	83.70	47.50	59.50	81.20	84.80	71.20	81.50	64.70	49.40	66.00	68.50
	ViT-L12×4	81.20	60.40	81.00	89.90	51.70	80.40	39.90	78.70	89.10	78.70	84.00	53.80	60.90	81.20	84.40	71.70	90.10	66.20	51.40	66.50	72.10
	ViT-H12×4	81.50	55.00	80.80	88.90	54.20	80.70	40.60	79.70	89.40	79.40	83.80	55.20	65.20	89.50	84.40	71.90	90.00	65.90	51.80	74.10	73.10
	ViT-G12×4	81.40	61.70	81.10	89.80	54.10	80.80	40.30	79.40	89.00	79.30	84.50	55.80	65.60	89.50	86.10	71.50	90.10	66.20	51.80	73.60	73.60

TABLE VII

THE DISTRIBUTION OF INSTANCES CORRESPONDING TO EACH CLASS FOR MEASURING SAMPLE EFFICIENCY USING THE DIOR-R DATASET. TO ENSURE THAT THE DATASET IS DIVIDED ACCURATELY BASED ON IMAGES, WE NEED TO VERIFY IF THE OBJECTS ARE DISTRIBUTED ACCORDING TO EACH RATIO. ALSO, THE SHORT NAMES FOR CATEGORIES ARE DEFINED AS SAME WITH TABLE V.

Sample ratio	The Number of Instance																				
	APL	APO	BF	BC	BR	CH	DAM	ETS	ESA	GF	GTF	HA	OP	SH	STA	STO	TC	TS	VE	WM	
1 %	13	8	22	5	17	7	7	7	10	3	14	16	25	260	6	37	50	7	247	19	
5 %	78	37	101	48	88	34	35	33	51	34	52	105	68	1195	32	216	220	22	766	136	
10 %	220	71	234	102	152	72	45	56	90	49	110	319	121	3040	59	282	601	44	1323	233	
50 %	965	325	1254	560	654	324	221	306	566	258	586	1244	633	13296	284	1730	2495	253	6858	1146	
100 %	1888	662	2384	1077	1367	649	512	610	1080	511	1162	2364	1330	27351	595	3042	4898	501	13725	2365	

the best performance possible.

B. Semantic Segmentation

1) *Dataset*: We evaluate pretrained models for the semantic segmentation downstream task using two benchmark datasets: Potsdam⁵ and LoveDA.

Potsdam. The Potsdam dataset, published by ISPRS, consists of 38 high-definition images with a pixel resolution of 0.5m. Each image has a fixed pixel size of 6000×6000 and is divided into 24 training images and 14 test images. This dataset is designed for semantic segmentation tasks, classifying six classes at the pixel level: impervious surfaces, buildings, low vegetation, trees, cars, and clutter. The evaluation criteria for the Potsdam dataset are the F1 score and overall accuracy, excluding the clutter category. The dataset is fully published, allowing models to be trained with training images and locally evaluated using test images.

LoveDA. The LoveDA dataset, designed for domain adaptation, features a pixel resolution of 0.3m and consists of

2522 training, 1669 validation, and 1796 test images. The dataset is divided into two areas, rural and urban, and includes seven classes: buildings, roads, water, barren land, forests, agriculture, and background. However, the background class is excluded during learning and evaluation. To demonstrate general performance, we construct the training and test datasets according to the official criteria, disregarding whether images are rural or urban. Unlike Potsdam, performance is estimated using the intersection over union (IoU) across all categories. Since only the test images are published, similar to DOTA v2.0, we evaluate our models by submitting the inference results to the server⁶.

2) *Implementation Details and Experiment Settings*: All experiments benchmarking the proposed backbone are performed using mmsegmentation⁷. As shown in subsection III-B, the intermediate features of layers 3, 6, 9, and 12 are resampled to achieve a ratio of 4, 2, 1, 0.5 through each scale block. Both datasets share the same hyperparameters, except for the training iteration. We train the semantic segmentation models

⁵<https://www.isprs.org/education/benchmarks/UrbanSemLab/2d-sem-label-potsdam.aspx>

⁶https://codalab.lisn.upsaclay.fr/competitions/421#learn_the_details-overview

⁷<https://github.com/open-mmlab/mmdetection>

TABLE VIII

THE RESULTS OF CLASS-WISE F1 SCORE, mF1 SCORE AND OVERALL ACCURACY (OA) ON POTSDAM. AS MENTIONED IN DATASET DETAIL, THE CLUTTER CLASS IS NOT INCLUDED TO EVALUATE THE PERFORMANCE. IN ORDER TO COMPARE THE RESULTS WITH THE ViTDETECT WITH OUT ANY MODULE SUCH AS ViTAE AND RVSA, \diamond IS THE RESULT RE-IMPLEMENTED IN MMSEGMENTATION FRAMEWORK USING THE VISION TRANSFORMER WEIGHT PUBLISHED BY [10].

Method	F1 score per category (%)					mF1 (%)	OA (%)
	Imper. surf.	Building	Low veg.	Tree	Car		
FCN [94]	88.61	93.29	83.29	79.83	93.02	87.61	85.59
PSPNet [111]	91.61	96.3	86.41	86.84	91.38	90.51	89.45
DeepLabV3+ [112]	92.35	96.77	85.22	86.79	93.58	90.94	89.74
UperNet [113]	93.14	96.75	86.3	86.13	91.56	90.78	91.26
S-RA-FCN [114]	91.33	94.7	86.81	83.47	94.52	90.17	88.59
UZ_1 [115]	89.3	95.4	81.8	80.5	86.5	86.7	85.8
UFMG_4 [116]	90.8	95.6	84.4	84.3	92.4	89.5	87.9
Multi-filter CNN [117]	90.94	96.98	76.32	73.37	88.55	85.23	90.65
HMANet [118]	92.38	96.08	86.93	88.21	95.44	91.81	90.46
LANet [119]	93.05	97.19	87.3	88.04	94.19	91.95	90.84
UperNet-SeCo [14]	91.21	94.92	85.12	84.89	89.02	89.03	89.64
UperNet(RSP-ViTAEv2-S) [57]	93.05	96.62	86.62	85.89	91.01	90.64	91.21
UperNet(ViT-B + RVSA) [10]	92.52	96.15	86.27	85.57	90.69	90.24	90.77
UperNet(ViTAE-B + RVSA) [10]	92.97	96.7	86.68	85.92	90.93	90.64	91.22
UperNet(ViT-B12 \times 1) \diamond [10]	91.04	96.56	83.34	88.13	95.29	90.87	91.12
UperNet(ViT-L12 \times 4)(Ours)	92.22	96.98	84.75	88.85	95.92	91.75	92.17
UperNet(ViT-H12 \times 4)(Ours)	92.73	96.92	85.64	88.85	95.99	92.02	92.54
UperNet(ViT-G12 \times 4)(Ours)	92.76	96.93	85.88	89.02	96.02	92.12	92.58

TABLE IX

THE RESULTS OF CLASS-WISE IOU AND mIoU ON LOVE DA. IN ORDER TO COMPARE THE RESULTS WITH THE ViTDETECT WITH OUT ANY MODULE SUCH AS ViTAE AND RVSA, \diamond IS THE RESULT RE-IMPLEMENTED IN MMSEGMENTATION FRAMEWORK USING THE VISION TRANSFORMER WEIGHT PUBLISHED BY [10].

Method	Intersection of Union (IoU)							mIoU
	Background	Building	Road	Water	Barren	forest	Argriculture	
FCN8S [94]	42.6	49.51	48.05	73.09	11.84	43.49	58.3	46.69
DeepLabV3+ [112]	42.97	50.88	52.02	74.36	10.4	44.21	58.53	47.62
PAN [120]	43.04	51.34	50.93	74.77	10.03	42.19	57.65	47.13
UNet [121]	43.06	52.74	52.78	73.08	10.33	43.05	59.87	47.84
UNet++ [122]	42.85	52.58	52.82	74.51	11.42	44.42	58.8	48.2
Unetformer [123]	44.7	58.8	54.9	79.6	20.1	46	62.5	46.9
Semantic-FPN [124]	42.93	51.53	53.43	74.67	11.21	44.62	58.68	48.15
PSPNet [111]	44.4	52.13	53.52	76.5	9.73	44.07	57.85	48.31
LinkNet [125]	43.61	52.07	52.53	76.85	12.16	45.05	57.25	48.5
FarSeg [126]	43.09	51.48	53.85	76.61	9.78	43.33	58.9	48.15
FactSeg [127]	42.6	53.63	52.79	76.94	16.2	42.92	57.5	48.94
HRNet [128]	44.61	55.34	57.42	73.96	11.07	45.25	60.88	49.79
UperNet(ViTAE-B + RVSA) [10]	46.69	58.14	57.12	79.66	16.55	46.46	62.44	52.44
UperNet(ViT-B12 \times 1) \diamond [10]	45.69	58.75	56.7	76.56	10.56	48.52	62.16	51.28
UperNet(ViT-L12 \times 4)	46.17	60.56	57.26	76.95	16.05	47.5	62.17	52.38
UperNet(ViT-H12 \times 4)	46.64	59.79	58.36	79.54	17.56	47.88	62.61	53.2
UperNet(ViT-G12 \times 4)	47.57	61.6	59.91	81.79	18.6	47.3	64	54.4

using the AdamW optimizer with a base learning rate of 0.00006 and weight decay of 0.01. The learning rate schedule applies the polynomial decay rule with a power of 1.0 and a minimum learning rate of 0. Additionally, linear warm-up is performed during the first 1,500 iterations with a ratio of 0.000001. We apply 160k and 80k training iterations for the Potsdam and LoveDA experiments, respectively. As with rotated object detection, we apply a 0.8 layer-wise learning rate decay and a drop path rate of 0.1 to ViTDETECT. The UperNet [113], a popular choice with vision transformer series, is used as the semantic segmentation head.

Since the Potsdam dataset has a fixed pixel size of 6000×6000 , we crop the training imagery into patches of size 512×512 with a stride of 384×384 . For the LoveDA dataset, with images of size 1024×1024 , we configure the data pipeline to randomly crop images into 512×512 patches. For both

datasets, we apply data augmentation sequentially, including resize and crop with a ratio range of 0.5 to 2.0, horizontal flip, and photometric distortion. To evaluate full scenes, we perform inference with patches of size 512×512 and a stride of 384×384 . For overlapped areas, we set the pixel class based on the average of logits.

3) *Experiment Results:* Tables Table VIII and Table IX present the semantic segmentation performance results for the Potsdam and LoveDA datasets, respectively. Table X demonstrates the improvement in data efficiency as the number of model parameters increases, with fine-tuning results on a reduced number of Potsdam samples. The best performance is indicated in red, while the second-best is in blue. We generate datasets with smaller portions by randomly selecting 1%, 5%, 10%, 50%, and 100% of the cropped images from the original dataset. The ratio of pixels representing each category is not

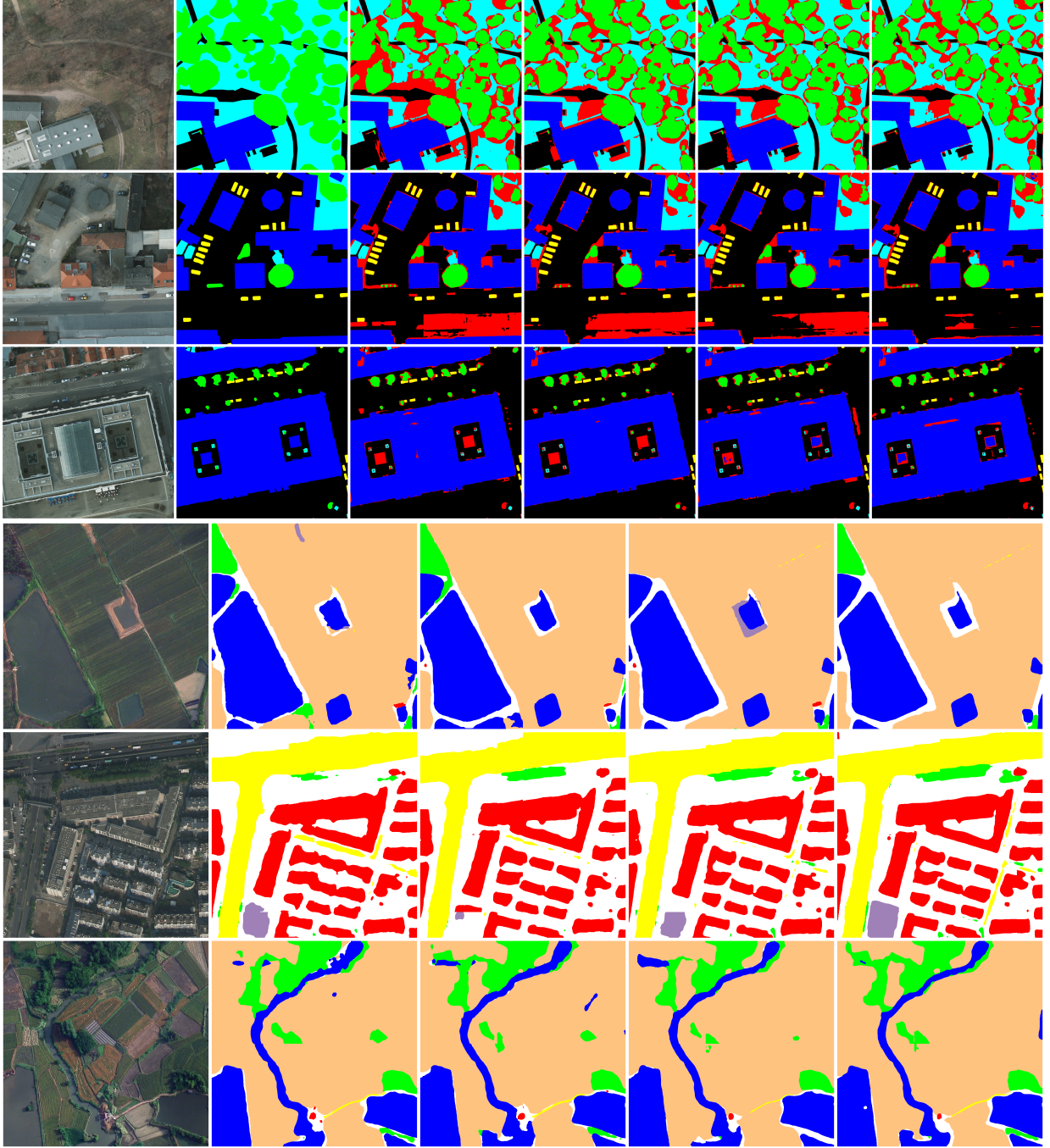


Fig. 6. Visualization results of the proposed model. The first to third rows are the results of the Potsdam dataset. The images from left to right are image, label, ViT-B12 \times 1, ViT-L12 \times 4, ViT-H12 \times 4, and ViT-G12 \times 4. The red color in Potsdam dataset means the false prediction. The fourth through sixth rows are the results of the LoveDA. Since the label of test dataset in LoveDA is unavailable, the images from left to right are image, ViT-B12 \times 1, ViT-L12 \times 4, ViT-H12 \times 4, and ViT-G12 \times 4.

TABLE X

THE RESULTS OF F1 SCORE, mF1 SCORE AND OVERALL ACCURACY (OA) FOR EVALUATING SAMPLE EFFICIENCY IN POTSDAM. IN ORDER TO COMPARE THE RESULTS WITH THE ViTDETR WITH OUT ANY MODULE SUCH AS ViTAE AND RVSA, THE ViT-B12×1 IS RETRAINED BY MMSEGMENTATION FRAMEWORK. THE TRAINING DATA OF POTSDAM IS RANDOMLY SAMPLED BY RATIO 0.01, 0.05, 0.1, 0.5, 1.0.

Sample ratio	Backbone	F1 score per category (%)					mF1 (%)	OA (%)
		Imper. surf.	Building	Low veg.	Tree	Car		
1%	ViT-B12×1 [10]	78.27	84.54	71.04	74.66	87.23	79.15	79.43
	ViT-L12×4	79.60	84.21	75.13	79.19	88.44	81.31	81.57
	ViT-H12×4	80.07	85.43	75.13	78.19	88.95	81.56	81.78
	ViT-G12×4	80.28	85.10	74.87	78.42	89.13	81.56	81.78
5%	ViT-B12×1 [10]	86.15	92.47	77.14	83.49	92.35	86.32	86.34
	ViT-L12×4	88.09	92.18	81.77	84.69	93.32	88.01	88.24
	ViT-H12×4	87.97	92.29	81.86	85.05	93.75	88.19	88.17
	ViT-G12×4	88.59	92.85	82.12	85.98	94.24	88.82	88.70
10%	ViT-B12×1 [10]	87.91	93.77	79.72	84.99	93.93	88.06	88.32
	ViT-L12×4	89.37	94.49	82.30	86.14	94.13	89.29	89.70
	ViT-H12×4	89.75	94.44	83.33	86.15	94.89	89.71	90.21
	ViT-G12×4	89.65	94.39	83.80	86.52	94.77	89.83	90.11
50%	ViT-B12×1 [10]	89.65	96.20	80.96	87.26	95.15	89.84	89.95
	ViT-L12×4	92.26	96.55	85.01	88.34	96.00	91.63	92.01
	ViT-H12×4	92.52	96.64	85.53	88.19	96.13	91.80	92.17
	ViT-G12×4	92.35	96.68	85.77	88.56	96.05	91.88	92.41
100%	ViT-B12×1 [10]	91.04	96.56	83.34	88.13	95.29	90.87	91.22
	ViT-L12×4	92.22	96.98	84.75	88.85	95.92	91.75	92.17
	ViT-H12×4	92.73	96.92	85.64	88.85	95.99	92.02	92.55
	ViT-G12×4	92.76	96.93	85.88	89.02	96.02	92.12	92.59

TABLE XI

THIS TABLE SHOWS THE DISTRIBUTION OF PIXEL CORRESPONDING TO EACH CLASS FOR MEASURING SAMPLE EFFICIENCY USING THE POTSDAM DATASET.

Sample ratio	The Number of Pixel				
	Imper. surf.	Building	Low veg.	Tree	Car
1 %	2480947	1945647	1903485	996186	109314
5 %	11201138	10877050	8637963	5901539	475325
10 %	22595456	20900276	18146952	11961627	1009088
50 %	112858442	113779095	93552823	58452932	5139681
100 %	227566256	222620959	187276028	119657591	10574847

accurately allocated, so for precise information on pixel ratios for each category, refer to Table XI.

Potsdam. Table VIII displays the F1 score, mF1 score, and overall accuracy (OA) for various models using the proposed backbone in Potsdam. As observed in the rotated object detection results, our proposed models outperform those pretrained by IMP in terms of mF1 score and overall accuracy. For the proposed models, a positive correlation exists between the number of parameters and both metrics, indicating that increasing the number of parameters tends to improve performance.

LoveDA. Table IX presents the intersection over union (IoU) results for LoveDA. Although the evaluation metric differs from that of the Potsdam dataset, the performance exhibits a similar pattern.

Sample Efficiency in Potsdam. To evaluate sample efficiency, an essential ability for foundation models in semantic segmentation, we conducted experiments on the Potsdam dataset using varying percentages of training data, including

1%, 5%, 10%, 50%, and 100%. As the dataset is partitioned based on images, the pixels corresponding to each class are not divided in an exact ratio. Table XI details the number of pixels representing each class included in each dataset. The models used for evaluating sample efficiency vary only in the backbone, with UperNet as the segmentation head. As observed, the model performance improves with an increase in the number of parameters while maintaining the same sample ratio. In many cases, using only half or a fifth of the dataset results in superior performance, as seen when comparing the 5% and 10% datasets to the 50% dataset.

V. CONCLUSION

In this study, we have demonstrated that a pretrained model with a vast number of parameters exhibits the essential capabilities expected from a foundation model in the field of modern deep learning. Our findings confirm the efficacy of fine-tuning and sample efficiency in crucial downstream tasks within the remote sensing domain, such as rotated object detection and semantic segmentation. Moreover, we have established that by employing parallelism in stacking the layers of a vision transformer, the resulting model effectively addresses tasks like rotated object detection and semantic segmentation. Consequently, our results indicate that a remote sensing-oriented foundation model can be achieved by pretraining a vision transformer with a large number of parameters on an extensive dataset of remote sensing images, coupled with the application of parallelism. Moving forward, our research aims to develop a remote sensing-oriented foundation model using an even more comprehensive collection of remote sensing images, including those from the MillionAID dataset. Furthermore, we plan to

investigate strategies for effectively controlling the foundation model through prompt tuning, few-shot learning, and fine-tuning methodologies.

ACKNOWLEDGMENT

This work was supported by Artificial intelligence industrial convergence cluster development project funded by the Ministry of Science and ICT (MSIT, Korea) & Gwangju Metropolitan City. The authors would like to thank Minseok Seo (SI Analytics) and Hakjin Lee (SI Analytics) for initial proofreading and valuable comments.

REFERENCES

- [1] J.-B. Grill, F. Strub, F. Altché, C. Tallec, P. Richemond, E. Buchatskaya, C. Doersch, B. Avila Pires, Z. Guo, M. Gheshlaghi Azar *et al.*, “Bootstrap your own latent—a new approach to self-supervised learning,” *Advances in neural information processing systems*, vol. 33, pp. 21 271–21 284, 2020.
- [2] T. Chen, S. Kornblith, K. Swersky, M. Norouzi, and G. E. Hinton, “Big self-supervised models are strong semi-supervised learners,” *Advances in neural information processing systems*, vol. 33, pp. 22 243–22 255, 2020.
- [3] M. Caron, H. Touvron, I. Misra, H. Jégou, J. Mairal, P. Bojanowski, and A. Joulin, “Emerging properties in self-supervised vision transformers,” in *Proceedings of the IEEE/CVF international conference on computer vision*, 2021, pp. 9650–9660.
- [4] J. Zhou, C. Wei, H. Wang, W. Shen, C. Xie, A. Yuille, and T. Kong, “ibot: Image bert pre-training with online tokenizer,” *arXiv preprint arXiv:2111.07832*, 2021.
- [5] K. He, X. Chen, S. Xie, Y. Li, P. Dollár, and R. Girshick, “Masked autoencoders are scalable vision learners,” in *Proceedings of the IEEE/CVF Conference on Computer Vision and Pattern Recognition*, 2022, pp. 16 000–16 009.
- [6] C. Jia, Y. Yang, Y. Xia, Y.-T. Chen, Z. Parekh, H. Pham, Q. Le, Y.-H. Sung, Z. Li, and T. Duerig, “Scaling up visual and vision-language representation learning with noisy text supervision,” in *International Conference on Machine Learning*. PMLR, 2021, pp. 4904–4916.
- [7] A. Radford, J. W. Kim, C. Hallacy, A. Ramesh, G. Goh, S. Agarwal, G. Sastry, A. Askell, P. Mishkin, J. Clark *et al.*, “Learning transferable visual models from natural language supervision,” in *International conference on machine learning*. PMLR, 2021, pp. 8748–8763.
- [8] P. Goyal, M. Caron, B. Leflaudeux, M. Xu, P. Wang, V. Pai, M. Singh, V. Liptchinsky, I. Misra, A. Joulin *et al.*, “Self-supervised pretraining of visual features in the wild,” *arXiv preprint arXiv:2103.01988*, 2021.
- [9] X. Zhai, A. Kolesnikov, N. Houlsby, and L. Beyer, “Scaling vision transformers,” in *Proceedings of the IEEE/CVF Conference on Computer Vision and Pattern Recognition*, 2022, pp. 12 104–12 113.
- [10] D. Wang, Q. Zhang, Y. Xu, J. Zhang, B. Du, D. Tao, and L. Zhang, “Advancing plain vision transformer towards remote sensing foundation model,” *IEEE Transactions on Geoscience and Remote Sensing*, 2022.
- [11] X. Sun, P. Wang, W. Lu, Z. Zhu, X. Lu, Q. He, J. Li, X. Rong, Z. Yang, H. Chang *et al.*, “Ringmo: A remote sensing foundation model with masked image modeling,” *IEEE Transactions on Geoscience and Remote Sensing*, 2022.
- [12] K. Ayush, B. Uzket, C. Meng, K. Tanmay, M. Burke, D. Lobell, and S. Ermon, “Geography-aware self-supervised learning,” in *Proceedings of the IEEE/CVF International Conference on Computer Vision*, 2021, pp. 10 181–10 190.
- [13] A. Ghanbarzade and H. Soleimani, “Self-supervised in-domain representation learning for remote sensing image scene classification,” *arXiv preprint arXiv:2302.01793*, 2023.
- [14] O. Manas, A. Lacoste, X. Giró-i Nieto, D. Vazquez, and P. Rodriguez, “Seasonal contrast: Unsupervised pre-training from uncurated remote sensing data,” in *Proceedings of the IEEE/CVF International Conference on Computer Vision*, 2021, pp. 9414–9423.
- [15] M. Dehghani, J. Djolonga, B. Mustafa, P. Padlewski, J. Heek, J. Gilmer, A. Steiner, M. Caron, R. Geirhos, I. Alabdulmohsin *et al.*, “Scaling vision transformers to 22 billion parameters,” *arXiv preprint arXiv:2302.05442*, 2023.
- [16] Y. Wang, C. M. Albrecht, and X. X. Zhu, “Self-supervised vision transformers for joint sar-optical representation learning,” in *IGARSS 2022-2022 IEEE International Geoscience and Remote Sensing Symposium*. IEEE, 2022, pp. 139–142.
- [17] Y. Cong, S. Khanna, C. Meng, P. Liu, E. Rozi, Y. He, M. Burke, D. B. Lobell, and S. Ermon, “Satmae: Pre-training transformers for temporal and multi-spectral satellite imagery,” *arXiv preprint arXiv:2207.08051*, 2022.
- [18] U. Jain, A. Wilson, and V. Gulshan, “Multimodal contrastive learning for remote sensing tasks,” *arXiv preprint arXiv:2209.02329*, 2022.
- [19] K. Cha, J. Seo, and Y. Choi, “Contrastive multiview coding with electro-optics for sar semantic segmentation,” *IEEE Geoscience and Remote Sensing Letters*, vol. 19, pp. 1–5, 2021.
- [20] G. Mikriukov, M. Ravanbakhsh, and B. Demir, “Deep unsupervised contrastive hashing for large-scale cross-modal text-image retrieval in remote sensing,” *arXiv preprint arXiv:2201.08125*, 2022.
- [21] K. Heidler, L. Mou, D. Hu, P. Jin, G. Li, C. Gan, J.-R. Wen, and X. X. Zhu, “Self-supervised audiovisual representation learning for remote sensing data,” *International Journal of Applied Earth Observation and Geoinformation*, vol. 116, p. 103130, 2023.
- [22] C. J. Reed, R. Gupta, S. Li, S. Brockman, C. Funk, B. Clipp, S. Candido, M. Uyttendaele, and T. Darrell, “Scale-mae: A scale-aware masked autoencoder for multiscale geospatial representation learning,” *arXiv preprint arXiv:2212.14532*, 2022.
- [23] X. X. Zhu, D. Tuia, L. Mou, G.-S. Xia, L. Zhang, F. Xu, and F. Fraundorfer, “Deep learning in remote sensing: A comprehensive review and list of resources,” *IEEE geoscience and remote sensing magazine*, vol. 5, no. 4, pp. 8–36, 2017.
- [24] E. Irwansyah and A. A. S. Gunawan, “Deep learning in damage assessment with remote sensing data: A review,” *Data Science and Algorithms in Systems: Proceedings of 6th Computational Methods in Systems and Software 2022*, Vol. 2, pp. 728–739, 2023.
- [25] L. Ma, Y. Liu, X. Zhang, Y. Ye, G. Yin, and B. A. Johnson, “Deep learning in remote sensing applications: A meta-analysis and review,” *ISPRS journal of photogrammetry and remote sensing*, vol. 152, pp. 166–177, 2019.
- [26] Z. Zheng, L. Lei, H. Sun, and G. Kuang, “A review of remote sensing image object detection algorithms based on deep learning,” in *2020 IEEE 5th International Conference on Image, Vision and Computing (ICIVC)*. IEEE, 2020, pp. 34–43.
- [27] X. Yuan, J. Shi, and L. Gu, “A review of deep learning methods for semantic segmentation of remote sensing imagery,” *Expert Systems with Applications*, vol. 169, p. 114417, 2021.
- [28] H. Su, S. Wei, S. Liu, J. Liang, C. Wang, J. Shi, and X. Zhang, “Hq-isnet: High-quality instance segmentation for remote sensing imagery,” *Remote Sensing*, vol. 12, no. 6, p. 989, 2020.
- [29] L. Khelifi and M. Mignotte, “Deep learning for change detection in remote sensing images: Comprehensive review and meta-analysis,” *Ieee Access*, vol. 8, pp. 126 385–126 400, 2020.
- [30] V. Risojević and V. Stojnić, “Do we still need imagenet pre-training in remote sensing scene classification?” *arXiv preprint arXiv:2111.03690*, 2021.
- [31] D. Marmanis, M. Datcu, T. Esch, and U. Stilla, “Deep learning earth observation classification using imagenet pretrained networks,” *IEEE Geoscience and Remote Sensing Letters*, vol. 13, no. 1, pp. 105–109, 2015.
- [32] R. Pires de Lima and K. Marfurt, “Convolutional neural network for remote-sensing scene classification: Transfer learning analysis,” *Remote Sensing*, vol. 12, no. 1, p. 86, 2019.
- [33] X. Liu, M. Chi, Y. Zhang, and Y. Qin, “Classifying high resolution remote sensing images by fine-tuned vgg deep networks,” in *IGARSS 2018-2018 IEEE International Geoscience and Remote Sensing Symposium*. IEEE, 2018, pp. 7137–7140.
- [34] A. Jaiswal, A. R. Babu, M. Z. Zadeh, D. Banerjee, and F. Makedon, “A survey on contrastive self-supervised learning,” *Technologies*, vol. 9, no. 1, p. 2, 2020.
- [35] F.-L. Chen, D.-Z. Zhang, M.-L. Han, X.-Y. Chen, J. Shi, S. Xu, and B. Xu, “Vlp: A survey on vision-language pre-training,” *Machine Intelligence Research*, vol. 20, no. 1, pp. 38–56, 2023.
- [36] Z. Gan, L. Li, C. Li, L. Wang, Z. Liu, J. Gao *et al.*, “Vision-language pre-training: Basics, recent advances, and future trends,” *Foundations and Trends® in Computer Graphics and Vision*, vol. 14, no. 3–4, pp. 163–352, 2022.
- [37] T. Chen, S. Kornblith, M. Norouzi, and G. Hinton, “A simple framework for contrastive learning of visual representations,” in *International conference on machine learning*. PMLR, 2020, pp. 1597–1607.

- [38] V. Stojnic and V. Risojevic, "Self-supervised learning of remote sensing scene representations using contrastive multiview coding," in *Proceedings of the IEEE/CVF Conference on Computer Vision and Pattern Recognition*, 2021, pp. 1182–1191.
- [39] H. Li, Y. Li, G. Zhang, R. Liu, H. Huang, Q. Zhu, and C. Tao, "Global and local contrastive self-supervised learning for semantic segmentation of hr remote sensing images," *IEEE Transactions on Geoscience and Remote Sensing*, vol. 60, pp. 1–14, 2022.
- [40] H. Chen, W. Li, S. Chen, and Z. Shi, "Semantic-aware dense representation learning for remote sensing image change detection," *IEEE Transactions on Geoscience and Remote Sensing*, vol. 60, pp. 1–18, 2022.
- [41] Y. Wang, C. M. Albrecht, N. A. A. Braham, L. Mou, and X. X. Zhu, "Self-supervised learning in remote sensing: A review," *arXiv preprint arXiv:2206.13188*, 2022.
- [42] K. He, X. Zhang, S. Ren, and J. Sun, "Deep residual learning for image recognition," in *Proceedings of the IEEE conference on computer vision and pattern recognition*, 2016, pp. 770–778.
- [43] A. Dosovitskiy, L. Beyer, A. Kolesnikov, D. Weissenborn, X. Zhai, T. Unterthiner, M. Dehghani, M. Minderer, G. Heigold, S. Gelly *et al.*, "An image is worth 16x16 words: Transformers for image recognition at scale," *arXiv preprint arXiv:2010.11929*, 2020.
- [44] Y. Long, G.-S. Xia, S. Li, W. Yang, M. Y. Yang, X. X. Zhu, L. Zhang, and D. Li, "On creating benchmark dataset for aerial image interpretation: Reviews, guidances, and million-aid," *IEEE Journal of selected topics in applied earth observations and remote sensing*, vol. 14, pp. 4205–4230, 2021.
- [45] J. Ding, N. Xue, G.-S. Xia, X. Bai, W. Yang, M. Y. Yang, S. Belongie, J. Luo, M. Datcu, M. Pelillo *et al.*, "Object detection in aerial images: A large-scale benchmark and challenges," *IEEE transactions on pattern analysis and machine intelligence*, vol. 44, no. 11, pp. 7778–7796, 2021.
- [46] G. Cheng, J. Wang, K. Li, X. Xie, C. Lang, Y. Yao, and J. Han, "Anchor-free oriented proposal generator for object detection," *IEEE Transactions on Geoscience and Remote Sensing*, vol. 60, pp. 1–11, 2022.
- [47] J. Wang, Z. Zheng, A. Ma, X. Lu, and Y. Zhong, "Loveda: A remote sensing land-cover dataset for domain adaptive semantic segmentation," *arXiv preprint arXiv:2110.08733*, 2021.
- [48] X. Liu, F. Zhang, Z. Hou, L. Mian, Z. Wang, J. Zhang, and J. Tang, "Self-supervised learning: Generative or contrastive," *IEEE Transactions on Knowledge and Data Engineering*, vol. 35, no. 1, pp. 857–876, 2021.
- [49] S. Albelwi, "Survey on self-supervised learning: auxiliary pretext tasks and contrastive learning methods in imaging," *Entropy*, vol. 24, no. 4, p. 551, 2022.
- [50] K. He, H. Fan, Y. Wu, S. Xie, and R. Girshick, "Momentum contrast for unsupervised visual representation learning," in *Proceedings of the IEEE/CVF conference on computer vision and pattern recognition*, 2020, pp. 9729–9738.
- [51] A. v. d. Oord, Y. Li, and O. Vinyals, "Representation learning with contrastive predictive coding," *arXiv preprint arXiv:1807.03748*, 2018.
- [52] X. Chen, H. Fan, R. Girshick, and K. He, "Improved baselines with momentum contrastive learning," *arXiv preprint arXiv:2003.04297*, 2020.
- [53] Z. Xie, Z. Zhang, Y. Cao, Y. Lin, J. Bao, Z. Yao, Q. Dai, and H. Hu, "Simmim: A simple framework for masked image modeling," in *Proceedings of the IEEE/CVF Conference on Computer Vision and Pattern Recognition*, 2022, pp. 9653–9663.
- [54] H. Bao, L. Dong, S. Piao, and F. Wei, "Beit: Bert pre-training of image transformers," *arXiv preprint arXiv:2106.08254*, 2021.
- [55] Z. Peng, L. Dong, H. Bao, Q. Ye, and F. Wei, "Beit v2: Masked image modeling with vector-quantized visual tokenizers," *arXiv preprint arXiv:2208.06366*, 2022.
- [56] C. Tao, J. Qi, M. Guo, Q. Zhu, and H. Li, "Self-supervised remote sensing feature learning: Learning paradigms, challenges, and future works," *arXiv preprint arXiv:2211.08129*, 2022.
- [57] D. Wang, J. Zhang, B. Du, G.-S. Xia, and D. Tao, "An empirical study of remote sensing pretraining," *IEEE Transactions on Geoscience and Remote Sensing*, 2022.
- [58] Y. Wang, C. M. Albrecht, N. A. A. Braham, L. Mou, and X. X. Zhu, "Self-supervised learning in remote sensing: A review," *IEEE Geoscience and Remote Sensing Magazine*, vol. 10, no. 4, pp. 213–247, 2022.
- [59] P. Bachman, R. D. Hjelm, and W. Buchwalter, "Learning representations by maximizing mutual information across views," *Advances in neural information processing systems*, vol. 32, 2019.
- [60] C. Tao, J. Qi, W. Lu, H. Wang, and H. Li, "Remote sensing image scene classification with self-supervised paradigm under limited labeled samples," *IEEE Geoscience and Remote Sensing Letters*, vol. 19, pp. 1–5, 2020.
- [61] C. J. Reed, X. Yue, A. Nrusimha, S. Ebrahimi, V. Vijaykumar, R. Mao, B. Li, S. Zhang, D. Guillory, S. Metzger *et al.*, "Self-supervised pretraining improves self-supervised pretraining," in *Proceedings of the IEEE/CVF Winter Conference on Applications of Computer Vision*, 2022, pp. 2584–2594.
- [62] G. Christie, N. Fendley, J. Wilson, and R. Mukherjee, "Functional map of the world," in *Proceedings of the IEEE Conference on Computer Vision and Pattern Recognition*, 2018, pp. 6172–6180.
- [63] Y. Yuan, L. Lin, Z.-G. Zhou, H. Jiang, and Q. Liu, "Bridging optical and sar satellite image time series via contrastive feature extraction for crop classification," *ISPRS Journal of Photogrammetry and Remote Sensing*, vol. 195, pp. 222–232, 2023.
- [64] Y. Chen and L. Bruzzone, "Self-supervised sar-optical data fusion of sentinel-1/2 images," *IEEE Transactions on Geoscience and Remote Sensing*, vol. 60, pp. 1–11, 2021.
- [65] Y. Wang, N. A. A. Braham, Z. Xiong, C. Liu, C. M. Albrecht, and X. X. Zhu, "Ssl4eo-s12: A large-scale multi-modal, multi-temporal dataset for self-supervised learning in earth observation," *arXiv preprint arXiv:2211.07044*, 2022.
- [66] P. Jain, B. Schoen-Phelan, and R. Ross, "Self-supervised learning for invariant representations from multi-spectral and sar images," *IEEE Journal of Selected Topics in Applied Earth Observations and Remote Sensing*, vol. 15, pp. 7797–7808, 2022.
- [67] —, "Multi-modal self-supervised representation learning for earth observation," in *2021 IEEE International Geoscience and Remote Sensing Symposium IGARSS*, 2021, pp. 3241–3244.
- [68] M. Huang, Y. Xu, L. Qian, W. Shi, Y. Zhang, W. Bao, N. Wang, X. Liu, and X. Xiang, "The qxs-saropt dataset for deep learning in sar-optical data fusion," *arXiv preprint arXiv:2103.08259*, 2021.
- [69] X. Lu, B. Wang, X. Zheng, and X. Li, "Exploring models and data for remote sensing image caption generation," *IEEE Transactions on Geoscience and Remote Sensing*, vol. 56, no. 4, pp. 2183–2195, 2017.
- [70] B. Qu, X. Li, D. Tao, and X. Lu, "Deep semantic understanding of high resolution remote sensing image," in *2016 International conference on computer, information and telecommunication systems (Cits)*. IEEE, 2016, pp. 1–5.
- [71] Z. Xia, Z. Li, Y. Bai, J. Yu, and B. Adriano, "Self-supervised learning for building damage assessment from large-scale xbd satellite imagery benchmark datasets," in *Database and Expert Systems Applications: 33rd International Conference, DEXA 2022, Vienna, Austria, August 22–24, 2022, Proceedings, Part I*. Springer, 2022, pp. 373–386.
- [72] X. Wanyan, S. Seneviratne, S. Shen, and M. Kirley, "Dino-mc: Self-supervised contrastive learning for remote sensing imagery with multi-sized local crops," *arXiv preprint arXiv:2303.06670*, 2023.
- [73] P. Jain, B. Schoen-Phelan, and R. Ross, "Self-supervised learning for invariant representations from multi-spectral and sar images," *IEEE Journal of Selected Topics in Applied Earth Observations and Remote Sensing*, vol. 15, pp. 7797–7808, 2022.
- [74] I. Goodfellow, J. Pouget-Abadie, M. Mirza, B. Xu, D. Warde-Farley, S. Ozair, A. Courville, and Y. Bengio, "Generative adversarial networks," *Communications of the ACM*, vol. 63, no. 11, pp. 139–144, 2020.
- [75] Y. Duan, X. Tao, M. Xu, C. Han, and J. Lu, "Gan-nl: Unsupervised representation learning for remote sensing image classification," in *2018 IEEE Global Conference on Signal and Information Processing (GlobalSIP)*. IEEE, 2018, pp. 375–379.
- [76] S. Singh, A. Batra, G. Pang, L. Torresani, S. Basu, M. Paluri, and C. Jawahar, "Self-supervised feature learning for semantic segmentation of overhead imagery," in *BMVC*, vol. 1, no. 2, 2018, p. 4.
- [77] Y. Yuan, L. Lin, Q. Liu, R. Hang, and Z.-G. Zhou, "Sits-former: A pre-trained spatio-spectral-temporal representation model for sentinel-2 time series classification," *International Journal of Applied Earth Observation and Geoinformation*, vol. 106, p. 102651, 2022.
- [78] Y. Yuan and L. Lin, "Self-supervised pretraining of transformers for satellite image time series classification," *IEEE Journal of Selected Topics in Applied Earth Observations and Remote Sensing*, vol. 14, pp. 474–487, 2020.
- [79] T. Brown, B. Mann, N. Ryder, M. Subbiah, J. D. Kaplan, P. Dhariwal, A. Neelakantan, P. Shyam, G. Sastry, A. Askell *et al.*, "Language models are few-shot learners," *Advances in neural information processing systems*, vol. 33, pp. 1877–1901, 2020.
- [80] A. Chowdhery, S. Narang, J. Devlin, M. Bosma, G. Mishra, A. Roberts, P. Barham, H. W. Chung, C. Sutton, S. Gehrmann *et al.*, "Palm: Scaling

- language modeling with pathways,” *arXiv preprint arXiv:2204.02311*, 2022.
- [81] L. Yuan, D. Chen, Y.-L. Chen, N. Codella, X. Dai, J. Gao, H. Hu, X. Huang, B. Li, C. Li *et al.*, “Florence: A new foundation model for computer vision,” *arXiv preprint arXiv:2111.11432*, 2021.
- [82] J. Deng, W. Dong, R. Socher, L.-J. Li, K. Li, and L. Fei-Fei, “Imagenet: A large-scale hierarchical image database,” in *2009 IEEE conference on computer vision and pattern recognition*. Ieee, 2009, pp. 248–255.
- [83] C. Sun, A. Shrivastava, S. Singh, and A. Gupta, “Revisiting unreasonable effectiveness of data in deep learning era,” in *Proceedings of the IEEE international conference on computer vision*, 2017, pp. 843–852.
- [84] A. Gupta, P. Dollar, and R. Girshick, “Lvis: A dataset for large vocabulary instance segmentation,” in *Proceedings of the IEEE/CVF conference on computer vision and pattern recognition*, 2019, pp. 5356–5364.
- [85] C. Schuhmann, R. Vencu, R. Beaumont, R. Kaczmarczyk, C. Mullis, A. Katta, T. Coombes, J. Jitsev, and A. Komatsuzaki, “Laion-400m: Open dataset of clip-filtered 400 million image-text pairs,” *arXiv preprint arXiv:2111.02114*, 2021.
- [86] W. Wang, H. Bao, L. Dong, J. Bjorck, Z. Peng, Q. Liu, K. Aggarwal, O. K. Mohammed, S. Singhal, S. Som, and F. Wei, “Image as a foreign language: Beit pretraining for all vision and vision-language tasks,” 2022.
- [87] H. Li, J. Zhu, X. Jiang, X. Zhu, H. Li, C. Yuan, X. Wang, Y. Qiao, X. Wang, W. Wang, and J. Dai, “Uni-perceiver v2: A generalist model for large-scale vision and vision-language tasks,” 2022.
- [88] H. Touvron, M. Cord, A. El-Nouby, J. Verbeek, and H. Jégou, “Three things everyone should know about vision transformers,” in *Computer Vision—ECCV 2022: 17th European Conference, Tel Aviv, Israel, October 23–27, 2022, Proceedings, Part XXIV*. Springer, 2022, pp. 497–515.
- [89] Y. Li, H. Mao, R. Girshick, and K. He, “Exploring plain vision transformer backbones for object detection,” in *Computer Vision—ECCV 2022: 17th European Conference, Tel Aviv, Israel, October 23–27, 2022, Proceedings, Part IX*. Springer, 2022, pp. 280–296.
- [90] J. Devlin, M.-W. Chang, K. Lee, and K. Toutanova, “Bert: Pre-training of deep bidirectional transformers for language understanding,” *arXiv preprint arXiv:1810.04805*, 2018.
- [91] A. Radford, J. Wu, R. Child, D. Luan, D. Amodei, I. Sutskever *et al.*, “Language models are unsupervised multitask learners,” *OpenAI blog*, vol. 1, no. 8, p. 9, 2019.
- [92] X. Chen, S. Xie, and K. He, “An empirical study of training self-supervised vision transformers,” in *Proceedings of the IEEE/CVF International Conference on Computer Vision*, 2021, pp. 9640–9649.
- [93] D. Hendrycks and K. Gimpel, “Gaussian error linear units (gelus),” *arXiv preprint arXiv:1606.08415*, 2016.
- [94] J. Long, E. Shelhamer, and T. Darrell, “Fully convolutional networks for semantic segmentation,” in *Proceedings of the IEEE conference on computer vision and pattern recognition*, 2015, pp. 3431–3440.
- [95] I. Loshchilov and F. Hutter, “Decoupled weight decay regularization,” *arXiv preprint arXiv:1711.05101*, 2017.
- [96] S. Rajbhandari, J. Rasley, O. Ruwase, and Y. He, “Zero: Memory optimizations toward training trillion parameter models,” in *SC20: International Conference for High Performance Computing, Networking, Storage and Analysis*. IEEE, 2020, pp. 1–16.
- [97] Y. Zhou, X. Yang, G. Zhang, J. Wang, Y. Liu, L. Hou, X. Jiang, X. Liu, J. Yan, C. Lyu *et al.*, “Mmrotate: A rotated object detection benchmark using pytorch,” in *Proceedings of the 30th ACM International Conference on Multimedia*, 2022, pp. 7331–7334.
- [98] J. Ding, N. Xue, Y. Long, G.-S. Xia, and Q. Lu, “Learning roi transformer for oriented object detection in aerial images,” in *Proceedings of the IEEE/CVF Conference on Computer Vision and Pattern Recognition*, 2019, pp. 2849–2858.
- [99] X. Xie, G. Cheng, J. Wang, X. Yao, and J. Han, “Oriented r-cnn for object detection,” in *Proceedings of the IEEE/CVF International Conference on Computer Vision*, 2021, pp. 3520–3529.
- [100] T.-Y. Lin, P. Goyal, R. Girshick, K. He, and P. Dollár, “Focal loss for dense object detection,” in *Proceedings of the IEEE international conference on computer vision*, 2017, pp. 2980–2988.
- [101] K. He, G. Gkioxari, P. Dollár, and R. Girshick, “Mask r-cnn,” in *Proceedings of the IEEE international conference on computer vision*, 2017, pp. 2961–2969.
- [102] K. Chen, J. Pang, J. Wang, Y. Xiong, X. Li, S. Sun, W. Feng, Z. Liu, J. Shi, W. Ouyang *et al.*, “Hybrid task cascade for instance segmentation,” in *Proceedings of the IEEE/CVF conference on computer vision and pattern recognition*, 2019, pp. 4974–4983.
- [103] G.-S. Xia, X. Bai, J. Ding, Z. Zhu, S. Belongie, J. Luo, M. Datcu, M. Pelillo, and L. Zhang, “Dota: A large-scale dataset for object detection in aerial images,” in *Proceedings of the IEEE conference on computer vision and pattern recognition*, 2018, pp. 3974–3983.
- [104] J. Dai, H. Qi, Y. Xiong, Y. Li, G. Zhang, H. Hu, and Y. Wei, “Deformable convolutional networks,” in *Proceedings of the IEEE international conference on computer vision*, 2017, pp. 764–773.
- [105] Y. Xu, M. Fu, Q. Wang, Y. Wang, K. Chen, G.-S. Xia, and X. Bai, “Gliding vertex on the horizontal bounding box for multi-oriented object detection,” *IEEE transactions on pattern analysis and machine intelligence*, vol. 43, no. 4, pp. 1452–1459, 2020.
- [106] G. Cheng, Y. Yao, S. Li, K. Li, X. Xie, J. Wang, X. Yao, and J. Han, “Dual-aligned oriented detector,” *IEEE Transactions on Geoscience and Remote Sensing*, vol. 60, pp. 1–11, 2022.
- [107] Y. Xu, Q. Zhang, J. Zhang, and D. Tao, “Vitae: Vision transformer advanced by exploring intrinsic inductive bias,” *Advances in Neural Information Processing Systems*, vol. 34, pp. 28 522–28 535, 2021.
- [108] Q. Zhang, Y. Xu, J. Zhang, and D. Tao, “Vitaev2: Vision transformer advanced by exploring inductive bias for image recognition and beyond,” *International Journal of Computer Vision*, pp. 1–22, 2023.
- [109] R. Bommasani, D. A. Hudson, E. Adeli, R. Altman, S. Arora, S. von Arx, M. S. Bernstein, J. Bohg, A. Bosselut, E. Brunskill *et al.*, “On the opportunities and risks of foundation models,” *arXiv preprint arXiv:2108.07258*, 2021.
- [110] Y. Kim, J. Oh, S. Kim, and S.-Y. Yun, “How to fine-tune models with few samples: Update, data augmentation, and test-time augmentation,” *arXiv preprint arXiv:2205.07874*, 2022.
- [111] H. Zhao, J. Shi, X. Qi, X. Wang, and J. Jia, “Pyramid scene parsing network,” in *Proceedings of the IEEE conference on computer vision and pattern recognition*, 2017, pp. 2881–2890.
- [112] L.-C. Chen, Y. Zhu, G. Papandreou, F. Schroff, and H. Adam, “Encoder-decoder with atrous separable convolution for semantic image segmentation,” in *Proceedings of the European conference on computer vision (ECCV)*, 2018, pp. 801–818.
- [113] T. Xiao, Y. Liu, B. Zhou, Y. Jiang, and J. Sun, “Unified perceptual parsing for scene understanding,” in *Proceedings of the European conference on computer vision (ECCV)*, 2018, pp. 418–434.
- [114] L. Mou, Y. Hua, and X. X. Zhu, “Relation matters: Relational context-aware fully convolutional network for semantic segmentation of high-resolution aerial images,” *IEEE Transactions on Geoscience and Remote Sensing*, vol. 58, no. 11, pp. 7557–7569, 2020.
- [115] M. Volpi and D. Tuia, “Dense semantic labeling of subdecimeter resolution images with convolutional neural networks,” *IEEE Transactions on Geoscience and Remote Sensing*, vol. 55, no. 2, pp. 881–893, 2016.
- [116] K. Nogueira, M. Dalla Mura, J. Chanussot, W. R. Schwartz, and J. A. Dos Santos, “Dynamic multicontext segmentation of remote sensing images based on convolutional networks,” *IEEE Transactions on Geoscience and Remote Sensing*, vol. 57, no. 10, pp. 7503–7520, 2019.
- [117] Y. Sun, X. Zhang, Q. Xin, and J. Huang, “Developing a multi-filter convolutional neural network for semantic segmentation using high-resolution aerial imagery and lidar data,” *ISPRS journal of photogrammetry and remote sensing*, vol. 143, pp. 3–14, 2018.
- [118] R. Niu, X. Sun, Y. Tian, W. Diao, K. Chen, and K. Fu, “Hybrid multiple attention network for semantic segmentation in aerial images,” *IEEE Transactions on Geoscience and Remote Sensing*, vol. 60, pp. 1–18, 2021.
- [119] L. Ding, H. Tang, and L. Bruzzone, “Lanet: Local attention embedding to improve the semantic segmentation of remote sensing images,” *IEEE Transactions on Geoscience and Remote Sensing*, vol. 59, no. 1, pp. 426–435, 2020.
- [120] H. Li, P. Xiong, J. An, and L. Wang, “Pyramid attention network for semantic segmentation,” *arXiv preprint arXiv:1805.10180*, 2018.
- [121] O. Ronneberger, P. Fischer, and T. Brox, “U-net: Convolutional networks for biomedical image segmentation,” in *Medical Image Computing and Computer-Assisted Intervention—MICCAI 2015: 18th International Conference, Munich, Germany, October 5–9, 2015, Proceedings, Part III* 18. Springer, 2015, pp. 234–241.
- [122] Z. Zhou, M. M. Rahman Siddiquee, N. Tajbakhsh, and J. Liang, “Unet++: A nested u-net architecture for medical image segmentation,” in *Deep Learning in Medical Image Analysis and Multimodal Learning for Clinical Decision Support: 4th International Workshop, DLMIA 2018, and 8th International Workshop, ML-CDS 2018, Held in Conjunction with MICCAI 2018, Granada, Spain, September 20, 2018, Proceedings 4*. Springer, 2018, pp. 3–11.
- [123] L. Wang, R. Li, C. Zhang, S. Fang, C. Duan, X. Meng, and P. M. Atkinson, “Unetformer: A unet-like transformer for efficient semantic

- segmentation of remote sensing urban scene imagery,” *ISPRS Journal of Photogrammetry and Remote Sensing*, vol. 190, pp. 196–214, 2022.
- [124] A. Kirillov, R. Girshick, K. He, and P. Dollár, “Panoptic feature pyramid networks,” in *Proceedings of the IEEE/CVF conference on computer vision and pattern recognition*, 2019, pp. 6399–6408.
 - [125] A. Chaurasia and E. Culurciello, “Linknet: Exploiting encoder representations for efficient semantic segmentation,” in *2017 IEEE visual communications and image processing (VCIP)*. IEEE, 2017, pp. 1–4.
 - [126] Z. Zheng, Y. Zhong, J. Wang, and A. Ma, “Foreground-aware relation network for geospatial object segmentation in high spatial resolution remote sensing imagery,” in *Proceedings of the IEEE/CVF conference on computer vision and pattern recognition*, 2020, pp. 4096–4105.
 - [127] A. Ma, J. Wang, Y. Zhong, and Z. Zheng, “Factseg: Foreground activation-driven small object semantic segmentation in large-scale remote sensing imagery,” *IEEE Transactions on Geoscience and Remote Sensing*, vol. 60, pp. 1–16, 2021.
 - [128] J. Wang, K. Sun, T. Cheng, B. Jiang, C. Deng, Y. Zhao, D. Liu, Y. Mu, M. Tan, X. Wang *et al.*, “Deep high-resolution representation learning for visual recognition,” *IEEE transactions on pattern analysis and machine intelligence*, vol. 43, no. 10, pp. 3349–3364, 2020.